Characterization and multifaceted anisotropy assessment of Corvio sandstone for geological CO_2 storage studies

by

Ismael Falcon-Suarez[2]

Jacobo Canal-Vila[1,3]

Jordi Delgado-Martin[1]

Laurence North[2]

&

Angus Best[2]

(1) Civil Engineering School. University of A Coruña. Campus de Elviña s/n 15071 A Coruña. Spain

(2) National Oceanography Centre, University of Southampton Waterfront Campus, European Way, Southampton, SO14 3ZH, UK

(3) Centro de Tecnología de Repsol Ctra. Extremadura, N-V Km 18, 28935 Móstoles. Spain

Manuscript submitted to:

Geophysical Prospecting

Date: August, 2015

Abstract

We present a comprehensive characterization of the physical, mineralogical, geomechanical, geophysical and hydrodynamic properties of Corvio sandstone. This information, together with a detailed assessment of anisotropy, is needed to establish Corvio sandstone as a useful laboratory rock-testing standard for well-constrained studies of thermo-hydro-mechanical-geochemical coupled phenomena associated with CO_2 storage practices and for geological reservoir studies in general. More than 200 core plugs of Corvio sandstone (38.1 and 50 mm diameter, 2:1 length to diameter ratio) were used in this characterization study, with a rock porosity of 21.7 ± 1.2%, dry density 2036 ± 32 kg m^{-3}, and unconfined compressive and tensile strengths of 41 ± 3.28 and 2.3 ± 0.14 MPa, respectively. Geomechanical tests show that the rock behaves elastically between ~10 and ~18 MPa under unconfined conditions with associated Young's modulus and Poisson's ratio of 11.8 ± 2.8 GPa and 0.34 ± 0.01, respectively. Permeability decreases abruptly with confining pressure up to ~10 MPa and then stabilizes at ~1 mD. Ultrasonic P- and S-wave velocities vary from about 2.8 to 3.8 km s^{-1} and 1.5 to 2.4 km s^{-1}, respectively, over confining and differential pressures between 0.1 - 35 MPa, allowing derivation of associated dynamic elastic moduli. Anisotropy was investigated using oriented core plugs for electrical resistivity, elastic wave velocity and attenuation, permeability and tracer injection tests. Corvio sandstone shows weak transverse isotropy (symmetry axis normal to bedding) of <10% for velocity and <20% for attenuation.

Key words: Corvio sandstone, weak anisotropy, wave velocities, strength, permeability, CO_2 storage, EOR.

1 Introduction

The injection of reactive fluids like CO_2 into geological formations for enhanced oil recovery (EOR) or carbon capture and storage (CCS) has been widely studied in the recent past. Before implementing CO_2 injection on large scale sites, it is crucial to assess the viability of the host geological strata. The main concern is that CO_2 injection could trigger a series of interlinked phenomena that affect the physical (or mechanical) and hydraulic properties of the reservoir, its seal, and even the cementing materials used in wellbores (Hangx *et al.* 2010; Kutchko *et al.* 2008; Liu *et al.* 2012; Rutqvist 2012; Song and Zhang 2012). Because water (brine) is always present in the rock pore space, the forced injection of CO_2 (whether in gas, liquid or supercritical state) induces significant acidification that leads to the onset of reactive processes, especially in the presence of carbonate or carbonate-bearing rocks (Le Guen et al. 2007; Gaus 2010; Vialle and Vanorio 2011). Siliciclastic formations are not expected to react significantly following the injection of CO_2–rich fluids, although the presence of lesser amounts of reactive minerals may play a significant role in their geological storage performance (Canal *et al.* 2013; Sim and Adam 2015). Hence, brine saturated sandstone reservoirs are the preferred targets for CO_2 storage because of their low reactive potential and high storage capacities.

The successful assessment of suitable reservoir formations relies heavily on an adequate understanding of the thermal, hydrodynamic, mechanical and geochemical (THMG) coupled processes that occur during injection and the resulting fluid-rock interactions. Typically, laboratory studies of reservoir and seal formation rocks are a major input to the assessment process. The limited availability (or even absence) of *in situ* samples is commonly solved by using rock analogues to the ones found in the target reservoir. A significant amount of literature can be found on the use of rocks

with well-known properties for conducting a range of laboratory tests (strength, permeability, etc.), to understand the behaviour of reservoir core flooding or to check instrument performance (Churcher *et al.* 1991). Also, in recent years, digital rock physics has evolved rapidly through the increasing resolution of X-ray computed tomography (CT) imaging , and has become a valuable tool for quick, non-destructive assessment of many rock properties (Andrä *et al.* 2013). However, these digital imaging techniques still require standard rock samples for calibration purposes and complementary destructive/non-destructive tests.

The specialist literature includes a wide number of reference rock materials used in many research works so that they now constitute *de facto* standard materials within the discipline of rock mechanics/rock physics. Among many other rocks, Berea sandstone (Krevor *et al.* 2012; Pini *et al.* 2012; Akbarabadi and Piri 2013; Nakagawa *et al.* 2013; Oh *et al.* 2013;), Tako sandstone (Xue and Ohsumi 2004; Xue and Lei 2006; Lei and Xue 2009; Nakatsuka *et al.* 2010) Bentheim sandstone (Klein *et al.* 2001), Bleurswiller sandstone (Fortin *et al.* 2005), Fontainebleau sandstone (Fredrich *et al.* 1993; Song and Renner 2008), Donnybrook sandstone (Mikhaltsevitch *et al.* 2014) and Navajo sandstone (Lu *et al.* 2011) have been used to investigate CO_2 injection in sandstone reservoirs, as well as for general reference materials in the petroleum industry. However, despite their widespread use and availability, none of them can be considered to be truly traceable standard materials because they display significant heterogeneity and anisotropy (although these are in themselves valid properties). Indeed, most sedimentary rocks of interest in exploration geophysics are considered to be weakly anisotropic, *i.e.,* with less than 20% anisotropy (Thomsen 1986). Sample heterogeneity is the greater problem because of what constitutes a representative laboratory sample volume for valid

upscaling of measured properties to large geological formations. The key point is that both heterogeneity and anisotropy must be accurately quantified for a valid standard material, not always achieved in the above mentioned works.

Sample anisotropy can be assessed from the contrast in P- and S- wave velocities propagating in directions orthogonal and parallel to bedding planes (Thomsen 1986; Wang 2002; Schubnel *et al.* 2006; Martínez and Schmitt 2013), and similarly for P- and S-wave attenuation (Q^{-1}, the reciprocal of the quality factor Q; Zhu and Tsvankin 2006; Best *et al.* 2007; Zhu *et al.* 2007; Chichinina *et al.* 2009). Electrical resistivity (Ellis *et al.* 2010) and magnetic susceptibility (*e.g.* Louis *et al.* 2004) have also been employed for this purpose. Although weak anisotropy can lead to negligible effects in some instances (Thomsen 1986), especially at the laboratory scale, it can be significant for the accurate calibration of geophysical techniques, fluid transport phenomena (*e.g.,* fingering) and when studying THMG coupled processes.

Corvio sandstone was chosen as a local reference material during the commissioning a CO_2 injection pilot plant in Northern Spain (Alcalde et al. 2014). In this paper, we present a comprehensive laboratory characterization of the properties of Corvio sandstone including anisotropy. The aims of this work is to summarize the most relevant physical, chemical, geomechanical and hydrodynamic properties of Corvio sandstone to provide a baseline database for subsequent studies, and to identify the extent and magnitude of anisotropy to inform studies of its possible impact on THMG coupled processes associated with CO_2 storage in siliceous sandstone reservoirs.

2 Materials and Methods

2.1 Corvio Sandstone

Corvio sandstone (CS) forms a c. 20 m thick unit (Corvio Formation) that appears in the top section of the Frontada Formation (Campoó Group; Lower Cretaceous) located in Northern Spain in the southern margin of the Basque-Cantabrian Basin. It is composed of siliceous sandstones and conglomerates. It displays decimetric to metric trough-type cross bedding associated with braided fluvial channels (Hernández *et al.* 1999). A total of 228 cylindrical plugs of diameter 38.1 and 50 mm, with an approximately length to diameter ratio of 2.0, were cored from four blocks (dimensions 0.3 x 0.2 x 0.5 m) of Corvio sandstone, orthogonally to the three independent surfaces of the sample block (arbitrarily denoted as X, Y, Z). Onwards, we denote samples as X-, Y- and Z-plugs to refer to the corresponding coring direction. The core plugs were carefully trimmed to meet geometric standards for rock mechanics studies (ISRM 1983).

2.2 Physical and chemical characterization

Knowledge of the physical and chemical properties of Corvio sandstone is important for CO_2 injection studies, since CO_2 is a reactive fluid whether in a liquid, gaseous or supercritical state. Hence, core chips were employed to determine mineralogy, density, porosity and pore size distribution.

The following techniques were used: X-ray diffraction and fluorescence (XRD and XRF; Siemens D5000 and Bruker-AXS S4 Pioneer, respectively); thermogravimetric analysis; differential thermal analysis and outgas analyses via Fourier transform infrared spectroscopy (TGA-DTA-FTIR; TA Inst. SDT 2960 coupled to Bruker Vector 22), which also provide information on water evaporation

mechanisms under controlled heating (Barrientos et al. 2010); Brunauer-Emmett-Teller (BET, Micromeritics Gemini VII 2390a) specific surface area; scanning electron microscopy coupled to energy dispersive microanalysis (SEM-EDS, JEOL JSM-6400); petrography (Olympus BX51); He pycnometry (Quantachrome Ultrapyc 1200e); Hg porosimetry (Quantachrome Poremaster-60); and X-Ray μCT-scans (XRadia MicroXCT-300). A total of 10 samples were used to assess the statistical significance of the measured properties.

2.3 Mechanical characterization

The long-term integrity of CO_2 repositories is linked to the potential mechanical deformation induced during the injection process. The mechanical stability of reservoirs is addressed through geomechanical modelling. The accuracy of these models depends on the available information about stresses and rock mechanical properties, based on geomechanical studies. This is crucial to identify the linear elasticity field from which static elastic moduli of the rock are calculated; but also to quantify deviations from perfect linear behaviour associated with compliant fractures and pores (Angus et al. 2010).

Geomechanical tests were performed on a total of 28 cylindrical plugs (diameter 50 mm; length to diameter ratio ~2) of Corvio sandstone, which were prepared to meet the recommendations of the International Society for Rock Mechanics (ISRM 1978; ISRM 1983): 11 for tensile strength (Brazilian test), 10 for unconfined compressive strength (UCS) and 6 for confined compressive strength (CCS).The tests were carried out using a MTS 815 testing system located at the facilities of the Rock Mechanics Laboratory (LaMEROC) of the University of A Coruña (Figure 1). During compressive strength tests, the axial strains were recorded with a dual-averaging knife-edge type extensometer, while the lateral strain

was measured using a circumferential chain-type extensometer. Some plugs were equipped additionally with four 350 Ω strain gages (two axial and two radial). Tensile strength was calculated indirectly (Brazilian test) by applying radial compression to induce tensile stresses in a thin discs of rocks (Bednárik and Kohút, 2012; Cai, 2010; Hakala et al., 2007).

Based on the measured stress-strain information, we computed the static elastic moduli according to ASTM (2007), and the critical stress states as presented in Hakala *et al.* (2007). Tangent Young's modulus (E) and Poisson's ratio (ν) were calculated at the strength level equal to 50% of UCS. The slope of the stress-strain curves was determined as the first derivative at a stress value equivalent to 50% of the peak strength, using a 3rd degree polynomial approximation. We also determined the characteristic stress levels describing the brittle behaviour of the rock, based on the work presented by Martin and Chandler (1994), further developed by Lau and Chandler (2004), Cai (2010) and Nicksiar and Martin (2012). These stress levels are known as crack closure stress (σ_{cc}), crack initiation stress (σ_{ci}), crack damage stress (σ_d) and failure (or peak) stress (σ_f). The crack closure stress corresponds to the load level up to which the strain occurs as a result of pore compaction and compliant crack closing.

2.4 Elastic waves

There is widespread use of seismic methods to monitor CO_2 movement and distribution in reservoir formations. Seismic properties of rocks are pressure-dependent, and so elastic wave velocities were measured on dry and water-saturated Corvio sandstone samples over a wide range of confining pressures, both under hydrostatic and non-hydrostatic conditions. These velocities were also

employed to compute the corresponding dynamic moduli (E_{dyn}, ν_{dyn}, K_{dyn} and μ_{dyn}) assuming isotropic homogeneous materials and standard relationships (*e.g.* Batzle *et al.* 2006; Rae *et al.* 2007).

Ultrasonic wave velocities (V_p, V_{s1} and V_{s2}*: P-wave, fast S-wave and slow S-wave, respectively*) were measured on 38.1 mm diameter core plugs with the aid of a pair of ErgoTech compression platens both equipped with one P-wave, and two orthogonally polarized S-wave, 1.3 MHz PZT transducers in pulse-transmission mode; time-of-flight was determined by picking first breaks (LaMEROC). The ultrasonic pulse-echo technique was used at the National Oceanography Centre, Southampton (NOC) on 50 mm diameter plugs, as presented in McCann and Sothcott (1992).

2.5 Permeability

Permeability is pressure-dependent and controls the rate of fluid advance through the reservoir formation. When mixed phase fluids (*e.g.*, brine and CO_2) are injected into a porous medium, the permeability to water (absolute permeability or hydraulic conductivity) is needed to calculate the relative permeability curves of the corresponding fluids. Hence, we measured the absolute permeability to water for different pairs of hydrostatic confining and pore fluid pressures. Permeability was determined by the steady state flow method (*i.e.,* Darcy's law) using water. We assumed a homogenous contribution to the flow of the full core cross-sectional area, and the absence of hydro-mechanical end-effects (Nguyen *et al.* 2013). In short, the ratio of volumetric flow rate, Q ($m^3\ s^{-1}$), to the pressure drop, ΔP (Pa), between the inlet and outlet of a sample of cross sectional area, A (m^2), and length, L (m), for a fluid dynamic viscosity, μ (Pa s), is related to absolute permeability, k (m^2), through the expression:

$$k = \frac{\mu L Q}{\Delta P A} \qquad (1)$$

The equipment used to conduct these tests combines a high pressure Hassler (LaMEROC) or Hoek-Franklin-type (NOC) core holders together with a number of high-pressure, high-resolution syringe pumps (ISCO 100DX, Quizix SP-5400, GDS ADVDPC) for maintaining confining pressure and fluid injection rates. Confining and pore pressure were continuously monitored with several pressure transducers (Keller-Drück series 33X). The system was configured to set a constant pore pressure gradient, while recording the flow rate upstream and downstream of the sample. For permeability calculations, only the steady flow condition was considered within a single step.

2.6 Anisotropy assessment

Assessing the potential of Corvio sandstone as a reference material requires an evaluation of how the main properties of the rock vary with orientation. Hence, we used a multicore approach similar to that described by Louis *et al.* (2004). We cored additional 38.1 and 50 mm diameter plugs orthogonal to the three independent surfaces of the sample block (arbitrarily denoted as X, Y, Z), trimmed to a length-to-diameter ratio of 2 and 0.4, respectively. Dry ultrasonic measurements were conducted at LaMEROC (pulse-transmission method) on long core plugs, including a set of measurements on three orthogonal plugs whereby the samples were rotated 20º stepwise around the longitudinal axial under minimum loading (~1 MPa) to ensure good coupling between the platen and sample. This results in 9 measurements per core plug and a total of 27 for the three X-, Y-, and Z-plugs. Long plugs were also used for permeability assessment and tracer injection tests.

Dry and fluid saturated short plugs were used for the pulse-echo technique at NOC for different combinations of confining and pore pressure. Short plugs were also employed to assess the dynamic coefficients, permeability and bulk electrical resistivity.

As a preliminary step, unconfined dry ultrasonic velocity was measured to assess weak anisotropy in the samples of interest. Based on these results, we designed two main sets of experiments to better characterize the observed anisotropy: (i) combined electrical resistivity, ultrasonic velocity and permeability on brine-saturated plugs under nearly hydrostatic confining conditions at NOC; (ii) tracer injection tests at LaMEROC.

P-wave velocity and attenuation, electrical resistivity and permeability were together analysed on three short orthogonal brine saturated samples using the experimental rig at NOC described in Falcon-Suarez *et al.* (2014). This rig employs a triaxial cell with a specially adapted rubber sleeve with a 16-electrode array, and bespoke data acquisition systems and software developed at the NOC. This enabled the determination of the full 9-component resistivity anisotropy tensor without bias from measurements on a single core sample (North *et al.* 2013; North and Best 2014). Because we employed a set of orthogonal plugs, we can also compare the equivalent isotropic resistivity by fitting a homogeneous, isotropic model to the resistivity data. This yields a crude estimate of the overall resistivity of the sample, although it must be acknowledged that this is biased by the geometry of the electrode array and the measurement protocol.

The combined electrical resistivity, ultrasonic P-wave velocity and attenuation, and permeability experiments (referred as RuVAK tests) were performed at room temperature on three 50 mm diameter, 20 mm length plugs (X-plug porosity $\phi = 0.23$;

Y-plug ϕ = 0.21; Z-plug ϕ = 0.22). The test procedure consisted of a drainage steady state flow test, setting a constant upstream flow of 0.5 cm^3 min^{-1} and a constant downstream pressure of 5 MPa. The pore fluid was 35 g L^{-1} NaCl brine solution. The test was repeatedly conducted for a loading/unloading path of differential pressure ($P_{diff} = \sigma_c - P_p$), by increasing the confining pressure 5 MPa stepwise from 10 to 25 MPa and back to 10 MPa, while keeping the P_p constant at 5 MPa. Furthermore, confining conditions were quasi-hydrostatic ($\sigma_1 - \sigma_3$ = 0.5 MPa) to emphasize the effect of the anisotropy along the longitudinal axis of each plug. For each loading/unloading step, a fluid volume of no less than 10 mL was circulated through the sample, corresponding to approximately one pore volume. Permeability was continuously monitored based on the final change in pore pressure gradient and corresponding flow.

The tracer tests performed were pulse-type (Shackelford *et al.* 1999; Ptak *et al.* 2004) and are referred to here as TPT tests. The tests used a brackish NaCl solution of 1000 μS cm^{-1} as injectate for the three 38.1 mm diameter X-, Y- and Z-plugs confined at 10 MPa under hydrostatic conditions. This confining pressure makes possible the closing of compliant cracks in order to better assess the relevance of small-scale porosity heterogeneities over fluid and solute transport. Rather than monitoring a chemical constituent, we continuously monitored the electrical conductivity of the effluent using a low-volume, flow-through, temperature-compensated conductivity sensor (MicroElectrodes Inc. mod. 8-900) coupled to a data acquisition system (ELIT 9705c Aqualyser) set to 1 Hz.

3 Results

3.1 Rock characterization

Corvio sandstone is light grey with occasional purple veins and has a medium grain size. It can be classified as a grain-supported quartzarenite with microcrystalline silica cement. The mineralogy of the Corvio sandstone is summarized in Table 1. Based on X-ray diffraction, the main mineral constituents are quartz (~94 wt. %) with subordinated kaolinite (~3.5 wt. %) and K-feldspar (~1.7 wt. %). Trace amounts of ilmenite (~0.2 wt. %) were observed in the μCT scans, while ~0.5 wt. % of carbonates, ~0.5 wt. % of hydrated minerals and <0.05 wt. % of C, N and S-compounds are inferred from the TGA-DTA-FTIR (Figure 2; weight loss sensitivity 0.1 μg or 0.0002%). The rock typically comprises sub-rounded quartz grains, is well sorted with an average grain size around 0.15 - 0.3 mm. In the studied samples, fossils comprised scarce cm-sized spots with remnants of tree debris (Hernández *et al.* 1999).

The average BET specific surface is 1.09 ± 0.07 $m^2 g^{-1}$ (n = 12) while porosity and dry density are 21.7 ±1.2 % (n = 224) and 2036 ±32 kg m^{-3} (n = 227) on average (Figure 3a - b). Available BET sorption/desorption isotherms show low hysteresis and correspond to the IUPAC's Type III (Rouquerol et al. 1994). This is typical of macroporous absorbents with weak surface affinity. The values obtained are comparable with that reported for the Berea (Zhan *et al.* 2010) and other sandstones.

From mercury porosimetry, we observed pore sizes from 0.1 to 1000 μm with a median pore size of ~20 μm (Figure 4a). Additionally, 3D and 2D-sections from the μCT-scanner (Figure 4b) revealed that, although pores tend to show an equant

shape, some larger open areas can be distinguished. These may lead to a compliant behaviour upon loading as confirmed by the stress-strain results presented below.

3.2 Rock strength and stress-strain behaviour

The mean tensile strength of Corvio sandstone is 2.3 ± 0.14 MPa, while UCS is 41.15 ± 3.28 MPa. Drained CCS values vary according with confining pressure (see Table 2). Figure 5 illustrates the corresponding strength envelope based on the Hoek-Brown model (Hoek and Brown 1980; Hoek *et al.* 2002) according to equation 2, which results in a m_b value of 13.2 by setting the *s* and *a* constants to 1 and 0.5, respectively (m_b, *s* and *a* are the Hoek-Brown material constants):

$$\sigma_1 = \sigma_3 + \sigma_c \left(m_b \frac{\sigma_3}{\sigma_c} + s \right)^a \qquad (2)$$

Static moduli were computed from the stress-strain curves from the UCS tests. For such conditions, the static Young's modulus (E) and Poisson's ratio (ν) are 11.8 ± 2.8 GPa and 0.34 ± 0.01, respectively; however, under confined conditions, E increases slightly (15.2 ± 2.8 GPa), while ν remains unchanged.

A further study of the stress levels presented by Corvio sandstone, shown in Figure 6, reveals that crack closure occurs up to a stress level, σ_{cc}, of 9.7 ± 1 MPa. With increasing stress, the rock shows elastic behaviour to a maximum value of 17.7 ± 2.3 MPa, which corresponds to the crack initiation stress, σ_{ci}; the crack damage onset stress, σ_d, initiates at 26.0 ± 2.4 MPa up to failure (*i.e.*, peak strength, σ_f). The peak strength of Corvio sandstone is consistently attained during the UCS tests at 41.15 ± 3.28 MPa under uniaxial conditions, although it rises to 222 MPa at 50 MPa confining pressure under dry conditions.

3.3 P- and S- wave velocities

V_p and V_s velocities were axially measured on 50 mm diameter X-plugs following a loading/unloading path from 0.5 to 35 MPa; the pressure steps were 2.5 and 5 MPa for non-hydrostatic and hydrostatic conditions, respectively. Figures 7a - b show wiggle-trace plots corresponding to the change in V_p and V_s of Corvio sandstone for 5 MPa steps, following the display used by Njiekak et al. (2013). We observe that, when increasing confining pressure, both velocities increase from 2.92 to 3.69 km s^{-1} and 1.51 to 2.09 km s^{-1}, respectively. Below 10 MPa, the loading effect follows an exponential curve consistent with the previously described crack closure stress stage, an effect that has been reported or inferred from experimental data in a number of works (Asef and Najibi 2013; King 1983; Mikhaltsevitch et al. 2014; Xu et al. 2006). The unloading path is slightly different from the loading one, with higher average velocities. This hysteresis is associated with irreversible damage suffered by the rock above the ~18 MPa limit associated with the crack initiation stress (Fortin et al. 2007; Xu et al. 2006).

Figures 8a - b illustrate the V_p and V_s curves obtained under non-hydrostatic conditions by increasing the axial load while keeping constant the radial confining pressure (*i.e.*, increasing the deviatoric stress). We observe that for low load (<10 MPa) and low confining pressure (0.1 MPa) there is a significant dependence of velocity with stress. This effect becomes less pronounced above 10 MPa loading, or at higher confining pressures. That means that closing of compliant cracks and pore compaction must be kept in mind when considering the ultrasonic characterization of plugs in the laboratory (Asef and Najibi 2013; King 1983).

Based on the previous elastic wave velocities and the dry density of the samples, we calculated the dynamic moduli of the rock: Young's modulus and

Poisson's ratio (E_{dyn} and ν_{dyn}; Figure 9a - b), and the bulk modulus and shear modulus (K_{dyn} and G_{dyn}; Figure 10a - b). Furthermore, comparing dynamic to static moduli we observe E_{dyn} is higher than E_{st} while ν_{dyn} is lower than ν_{st}, which has been largely identified in the past (Asef and Najibi 2013; Eissa and Kazi 1988; King 1983; Fjær 2009). The reasons for such differences include the properties of the pore fluid, frequency of cracks, the stress path and the inherent difference of strain amplitudes between static and dynamic (at ultrasonic frequencies) methods (Blake and Faulkner 2016; Fjær et al. 2013). In our case, the static moduli are determined at the stress level equal to 50% of UCS, laying above the elastic limit of the rock in all the cases. In this regard, the use of one single UCS test to determine the sensitivity of static moduli to the stress level could be inaccurate, and further studies applying damage controlled tests as those used by Fjær (2009) or Lau and Chandler 2004), might improve our correlation between static and dynamic moduli.

3.4 Permeability

The permeability of 38.1 mm diameter X-type plugs was evaluated with a series of 4 consecutive steady state flow tests performed along step wise loading/unloading cycles (between 5 and 30 MPa of hydrostatic confining pressure, *i.e.*, $\sigma_c = \sigma_1 = \sigma_2 = \sigma_3$). Each one has a constant pore pressure (P_p, from 1 to 16 MPa), which is increased from one to the next to repeat the differential stress sequence ($P_{diff} = \sigma_c - P_p$). Figure 11 shows that permeability progressively varies from 4 to 0.8 mD (~$8 \cdot 10^{-16}$ to ~$4 \cdot 10^{-15}$ m^2) while increasing confining pressure. There is a significant drop in permeability once the first loading/unloading cycle is completed, thought to be associated with pore closing and crack compliance. The permeability change after the 2nd, 3rd and 4th loading/unloading cycles is much smaller, although the P_{diff} is kept constant along the sequence, which provides further evidence of the permanent

deformation of the sample during initial loading due to pore closure. Hysteresis upon unloading is relatively small, below 15%. Overall, the observed permeability evolution can be attributed to compaction of pore space and favourably oriented cracks, already documented in other sandstones (Bernabé 1991; Zhu and Wong 1996; Ojala *et al.* 2004).

4 Anisotropy assessment

4.1 Exploratory approach

None of the 4 Corvio sandstone blocks, from which core plugs were taken, displayed any clear evidence of heterogeneity (especially cross bedding), and that was also the case for the small scale μCT X-ray scans. To further investigate the existence of anisotropy, we performed an exploratory survey with the plugs sampled orthogonally to the three independent surfaces (denoted as X, Y and Z) of the parallelepiped sandstone block. Figure 12 shows the vector-distribution of V_p, V_{s1} and V_{s2} (transverse to V_{s1}) resulting from the non-saturated unconfined test in which three X-, Y- and Z-plugs were revolved in steps of 20º around their longitudinal axes. Calculations show that V_p and V_s (average of V_{s1} and V_{s2}) are 2986 ±18 and 1515 ± 32 m s^{-1} for the X-plug; 3289 ± 48 and 1716 ± 21 m s^{-1}, for the Y-plug; and 3360 ± 32 and 1729 ± 20 m s^{-1}, for the Z-plug. Hence, V_p in the longitudinal direction of the X-plug is ~10% slower than in the Z-plug, and ~8% slower than in the Y-plug. Similarly, V_s is about 12% slower in both the Y- and Z-plugs. Further observation of the same figure lets us conclude that the rock is transversely isotropic in the longitudinal direction of Z-plugs, since the P and S-wave velocities are relatively insensitive to rotation, while the X- and Y-plugs are slightly orthotropic. It is worth noting that the X-plug shows 90º crossed symmetric values, indicating some sort of preferential void alignment perpendicular to the axis. Besides, the difference

between Vs1 and Vs2 is a proof of anisotropy, since different velocities along different wave paths may imply heterogeneity. The case of the Y-plug is more difficult to explain since V_p should be unaffected by axial rotation, but the results show the contrary (V_p is higher at 45º).

4.2 RuVAK tests analysis

Figure 13a - b show the P- and S wave velocities and corresponding attenuation coefficients for the three plugs and how they change with differential pressure (P_{diff}). As observed in the first exploratory assessment, the X-plug displays the lowest V_P and V_S while the smaller attenuations (Q_p^{-1} and Q_s^{-1}) correspond to the Z-plug. Attenuations for X- and Y-plugs show, however, similar values. In all the RuVAK tests, the three samples display consistent trends and similar slight hysteresis upon unloading, which suggests a *quasi*-isotropic mechanical behaviour. This behaviour is inferred from V_p and Q_p^{-1} against bulk electrical resistivity (*ER;* Figure 14), where the three plugs display parabolic trends with parallel symmetry axes (*i.e.,* constant V_p:*ER* and Q_p^{-1}:*ER* ratios). Likewise, *ER* seems to be relatively unaffected by stress-strain (<10% for an increment of 15 MP in P_{diff}) when compared to wave velocities, possibly because of the relatively high porosity of the rock (*i.e.*, most ionic flow is through large open pores, and relatively insensitive to pressure-dependent crack-related flow); *ER* is expected to be more sensitive to pore fluid electrical conductivity changes. This observation is highly relevant when considering reactive transport phenomena which imply changes in the electrical conductivity of the fluid or the replacement of the resident fluid by some other, for instance CO_2 (*e.g.* Alemu *et al.* 2013).

Figure 15 shows the change in resistivity and permeability during the RuVAK tests performed with the oriented plugs. We observe that both parameters slightly

vary with P_{diff} (<10%) and, as expected, they show opposite trends, *i.e.*, pore compliance results in an increase in ER but a decrease in permeability. However, the relative difference among the three directions reaches ~18% for *ER* and up to 80% for permeability, with the plane defined by the X- and Z-plugs showing the greatest degree of anisotropy. The permeability values obtained during the RuVAK tests coincides with the previous assessments when P_{diff} and σ_c are above 5 and 10 MPa, respectively (Figure 11). The X-and Z-plugs have the highest and lowest permeability values, respectively, although the difference between them is of the order of 1 mD. Following the transverse isotropy (TI) model, permeability is lower in the direction perpendicular to the bedding surface (*i.e.*, X-plug). The minimum permeability in this direction is related to a more variable grain size distribution, compaction and pore collapse during burial (Farrell *et al.* 2014). Similarly, the lowest *ER* is also orthogonal to bedding, which is in agreement with the data reported by North and Best (2014) for other sedimentary rocks. The same authors have also reported that *ER* anisotropy in sandstones may reach up to 25%, emphasizing the possible importance of anisotropy on the assessment of CO_2 storage reservoirs.

The *ER* anisotropy has been further analysed by using the approach described in North and Best (2014). The process to extract anisotropy from the raw data is based on an algorithm that tries to fit a uniformly anisotropic forward model to the ER observations, unbiased by preconceptions of the symmetry of anisotropy or the orientation of the sample. Figure 16 illustrates the 3D anisotropy tensor ellipsoid (*i.e.*, the full 9-component resistivity tensor) associated with the measurements performed on each orthogonal plug. In the ideally isotropic case, observations made on reciprocal pairs should coincide (*e.g.,* $Z_x = X_z$). However, because we induced a small deviatoric stress of 0.5 MPa to emphasize anisotropy evidences, the results

are slightly biased along the axial component of each plug. Nonetheless, the high degree of sphericity and the small variation of resistivity in absolute terms show that the rock is only very slightly anisotropic.

Based on sedimentary fabric models presented by North *et al.* (2013), we interpret the presence of the following sedimentary structures in Corvio sandstone: (i) the X-plugs have bedding orthogonal to the axis of the plug; (ii) the Y-plugs have tubular micro-structure slightly oblique to the axis of the plug; and (iii) the Z-plugs have laminated micro-structure along the axis of the plug. Based on all the previous information, we infer the presence of a weak cross-bedding structure that would somehow reflect the macroscale cross bedding previously reported for the Corvio sandstone by Hernández *et al.* (1999).

The tracer TPT tests also provide an alternative mean to test the anisotropy of Corvio sandstone. These tests are significant as they directly emphasize the transport properties of the rock, providing information about actual flow-paths and fluid-flow through. Hence, it is possible to obtain information on the pore space (and transport properties) of the rock from the shape of the breakthrough curve (Ptak *et al.* 2004). It is far from the scope of this contribution to provide a detailed assessment of TPT tests although some general ideas can be presented. Assuming that the movement of the tracer conforms to piston-type flow, the injection of a discrete stepped pulse at the inlet of the sample translates into a tailed bell-shape breakthrough curve at its outlet (Fetter 1993). The change from a squared to a, more or less pronounced, tailed bell-shape curve depends on the relative importance of diffusive/dispersive effects while the tracer is crossing the pore space of the sample.

The tracer injection tests were repeated up to five times for the X-, Y- and Z-plugs, obtaining comparable results in each case. Representative breakthrough

curves are illustrated in Figure 17. From a merely descriptive point of view, we see in our experiments that the faster travel time occurs for the Y-plug and is followed by the Z- and X-plugs. The relative height of the peak conductivity has the opposite order (highest for the X-plug and lowest for the Y-plug). Because electrical conductivity is a conservative tracer in our test (were chemical reactions are negligible according to the mineralogy of the rock, at the time-scale of the test) the surface area covered by each breakthrough curve is nearly identical.

Permeability results show that the plug showing the lowest value was the X-plug. This is consistent with the slowest arrival time of the same orientation in the TPT tests. However, the Y-plug has lower k than the Z-plug which is in apparent contradiction with the TPT results from the same plugs. Furthermore, if we focus on the shape of the Y-plug breakthrough curve, the recession curve shows a protuberance (*i.e.*, the trailing limb after the peak value) which points towards a double-porosity system. One porosity, well connected, would contribute providing fast trackways for tracer transport (also responsible for the early breakthrough) and a second one, less well connected, providing a delayed arrival of tracer with a peak value (the first inflexion point in the recession curve) located between the peak times for the X- and Z-plugs. The double porosity effect on permeability is imperceptible since the measurements are conducted in a constant flow mode, so dominated by preferential path flows (primary porosity), instead of a single pulse (TDT tests). Nonetheless, such a feature is consistent with our previous interpretation of weak cross-bedding.

4.3 Weak anisotropy assessment: detailed approach

The previous results encouraged the development of a more detailed anisotropy investigation. Based on these, we assumed that Corvio sandstone is

transversely isotropic (TI), allowing the application of weak anisotropy formulae (Thomsen 1986). Accordingly, since V_p is normally lower in the direction perpendicular to bedding (King 2009; Martínez and Schmitt 2013; Thomsen 1986; Wang 2002), the direction along the X-plug (or vector V) would correspond to the symmetry axis, while the isotropic plane containing the Y- and Z-plugs axial directions (with velocities about 10% higher) defines the bedding plane (*i.e.*, two perpendicular directions to the anisotropy symmetry axis H_1 and H_2). Then, taking the Thomsen's (1986) notation and equations, it is possible to evaluate the anisotropy for P-wave velocity (ε) and *S-wave velocity* (γ) from four of the five elastic constants of the material (C_{11}, C_{33}, C_{44} and C_{66}) as follows:

$$\varepsilon = \frac{C_{11} - C_{33}}{2C_{33}} \qquad (3)$$

$$\gamma = \frac{C_{66} - C_{44}}{2C_{44}} \qquad (4)$$

where $C_{11} = \rho V_{p(H1,2)}^2$; $C_{33} = \rho V_{p(V)}^2$; $C_{66} = \rho V_{s(H1,2)}^2$; and $C_{44} = \rho V_{p(V)}^2$. A more detailed explanation of the notation and equations is given in Thomsen (1986), Wang (2002) and Louis *et al.* (2004). It is worth noting that we independently compute ε and γ for H_1 and H_2 (*i.e.,* Y- and Z-plugs) since both directions are orthogonal to the symmetry axis. In this study we lack a sample cored at 45º, hence the third Thomsen's anisotropy parameter δ (Thomsen 1986) cannot be calculated. Likewise, to analyse the anisotropy of the rock in terms of P- and S-wave attenuations (Q_p^{-1} *and* Q_s^{-1}), we use the Thomsen-style parameters proposed by Zhu and Tsvankin (2006), as presented in Best *et al.* (2007):

$$\varepsilon_Q = \frac{Q_p^{-1}(H_{1,2}) - Q_p^{-1}(V)}{Q_p^{-1}(V)} \quad (5)$$

$$\gamma_Q = \frac{Q_s^{-1}(H_{1,2}) - Q_s^{-1}(V)}{Q_s^{-1}(V)} \quad (6)$$

The computed velocity and attenuation anisotropies are represented in Figure 18a - b, as ε, γ, ε_Q, γ_Q percentages versus differential stress. The P- and S- wave velocity anisotropy parameters ε and γ display similar evolution versus P_{diff}, decreasing from 12 to 8% and 8 to 4%, respectively, when P_{diff} increases 15 MPa. Furthermore, the changes of ε and γ in the plane defined by the X- and Y-plugs (ε_{xy} and γ_{xy}) are less pronounced (*i.e.,* less anisotropic) than those observed for the plane defined by the X- and Z-plugs (ε_{xz} and γ_{xz}); this suggests that pore compaction is more significant along the former plane. Additionally, the low hysteresis observed at the end of the unloading path (~2%) would suggest that the reduction of anisotropy due to compression is largely controlled by the compliance of equant pores. In this regard, the non-linear trends are likely indicating that microcrack-closing is also playing a role (Martínez and Schmitt 2013). Nevertheless, our data suggest that all core plugs evolve to a more isotropic state when confining pressure is increased as ε and γ tend to decrease.

The attenuation parameters (ε_Q and γ_Q) show similar trends to those described previously for velocities, although ε_Q is positive (<12%) and γ_Q negative (20 – 25%). The parameter γ_Q ranges between -5 to 5% for the plane defined by the X- and Y-plugs, and stays around -10% for that defined by the X- and Z-plugs, without showing a clear dependence on P_{diff}. As noted by Best *et al.* (2007), for P_{diff} increments greater than those used in this study, attenuation anisotropy in

sandstones is more sensitive to pressure changes than velocity anisotropy. So that P- and S-wave attenuation parameters provide more information about the magnitude of the anisotropy. Nonetheless, whether the velocity or attenuation anisotropy is considered, Corvio sandstone seems to be weakly anisotropic according to Martinez and Schmitt (2013).

5 Summary and conclusions

We have reported a comprehensive characterization for Corvio sandstone and paid special attention to the assessment of weak anisotropy from a multifaceted perspective. The average mineralogy is dominated by quartz (~94%), kaolinite (~3.5%) and k-feldspar (~1.7%), which suggests low chemical reactivity when submitted to the injection of CO_2 or CO_2-saturated fluids, at least on short time scales. This is useful when trying to focus on thermo-hydro-mechanical processes associated to CO_2 injection with minimum impact of chemical processes.

The standard geomechanical characterization also provides relevant information. The crack closing stress (which refers to pore compaction and compliant crack closing) occurs at 10 MPa while the onset of crack initiation occurs at ~18 MPa. These values have been indirectly verified by different techniques. Direct application of these results implies better assessment of experimental conditions in order to reduce undesired effects like enhanced permeability due to non-closed cracks at low stress levels, or associated with rock damage induced by high stresses.

The average permeability of Corvio sandstone varies from 4 to 0.8 mD, decreasing with confining pressure. It is worth noting that, within the studied testing range, the main process inducing hysteresis in the rock (reflected in the

hydrodynamic and velocity responses) is related to pore compaction and compliant crack closure below 10 MPa.

Although no sedimentary structures were detected at block-scale or through the X-ray μCT-scans, we have developed a multifaceted anisotropic analysis (multicore analysis), concluding that Corvio sandstone is weakly anisotropic: ultrasonic P-wave velocity anisotropy is <12% (<8% for the S-wave), attenuation anisotropy is < 20%, electrical resistivity varies <18% with plug orientation and permeability slightly oscillates (±1 mD) depending on the direction considered. Nonetheless, the anisotropy is again more significant within the crack closure domain, emphasising the importance of considering this mechanical limit when interpreting rock behaviour during hydromechanical studies. In addition, the bulk electrical resistivity analysis and the tracer injection tests both infer the presence of weak cross-bedding.

These characterization results constitute a useful baseline for CO_2 injection studies using this sedimentary rock. Our results are of direct application when working with this rock in the laboratory, as they help us: (i) to understand non-obvious processes such as thresholds for pore compaction, compliant crack closure, and physicochemical coupling; (ii) to better calibrate geophysical techniques by reducing uncertainty and providing a well-constrained fabric model; (iii) to improve experimental design parameters such as stress ranges, plug orientation, and vector properties, among others. Furthermore, we want to highlight the importance of weak anisotropy when considering naturally homogeneous materials (at least in appearance). These observations can be scaled up to field scenarios in order to improve reservoir models.

This comprehensive characterization of Corvio sandstone covers geomechanical, geochemical, geophysical and hydrodynamic properties. Together

with the detailed assessment of anisotropy presented here, the results indicate that Corvio sandstone could be used as a particularly interesting rock-standard to improve the understanding of reservoirs subjected to complex thermo-hydro-mechano-geochemical coupled phenomena, typically associated with CO_2 storage practices.

Acknowledgments

Some of the measurements reported here were performed at the esCO_2–CIUDEN facilities (OXY CFB 300 Compostilla Project) and the Colorado School of Mines. Assistance and advice of Drs. T. Kovacs, M. Batzle, V. Barrientos, B. Rodriguez, K. Amalokwu and Gaye Bayrkci are kindly acknowledged. Funds for this work have been provided by the XUGA Project 10REM003CT and the European Regional Development Funds 2007/2013. Additional support was provided by UK EPSRC grant EP/K035878/1 and the UK Natural Environment Research Council. This work is dedicated to the memory of Dr. Mike Batzle. Data presented in this study are available at the PANGAEA database (http://www.pangaea.de).

References

Alcalde J., Marzán I., Saura E., Martí D., Ayarza P., Juhlin C., Pérez-Estaún A., Carbonell R. 2014. 3D geological characterization of the Hontomín CO_2 storage site, Spain: Multidisciplinary approach from seismic, well-log and regional data. Tectonophysics 627, 6-25.

Akbarabadi M. and Piri M. 2013. Relative permeability hysteresis and capillary trapping characteristics of supercritical CO_2/brine systems: An experimental study at reservoir conditions. Advances in Water Resources, 52, 190-206.

Alemu B.L., Aker E., Soldal M., Johnsen Ø. and Aagaard P. 2013. Effect of sub-core scale heterogeneities on acoustic and electrical properties of a reservoir rock: a CO_2 flooding experiment of brine saturated sandstone in a computed tomography scanner. Geophysical Prospecting, 61, 235-250.

Andrä H., Combaret N., Dvorkin J., Glatt E., Han J., Kabel M., Keehm Y., Krzikalla F., Lee M., Madonna C., Marsh M., Mukerji T., Saenger E.H., Sain R., Saxena N., Ricker S., Wiegmann A. and Zhan X. 2013. Digital rock physics benchmarks—Part I: Imaging and segmentation. Computers & Geosciences, 50, 25-32.

Angus D.A., Kendall J.M., Fisher Q.J., Segura J.M., Skachkov S., Crook A.J.L. and Dutko M. 2010. Modelling microseismicity of a producing reservoir from coupled fluid-flow and geomechanical simulation. Geophysical Prospecting, 58, 901-914.

Asef, M.R. and Najibi, A.R. 2013. The effect of confining pressure on elastic wave velocities and dynamic to static Young's modulus ratio. Geophysics, 78, D135-D142.

ASTM 2007. Standard Test Method for Compressive Strength and Elastic Moduli of Intact Rock Core Specimens under Varying States of Stress and Temperatures; D7012:2007 Annual Book of ASTM Standards, Section 4: Construction, Volume 04.09: Soil and Rock (II), ASTM International, West Conshohocken (PA), pp. 1429-1436.

Batzle M.L., Han D.H. and Hofmann R. 2006. Fluid mobility and frequency-dependent seismic velocity-Direct measurements. Geophysics, 71, N1-N9.

Barrientos V., Delgado J., Navarro V., Juncosa R., Falcón I. and Vázquez A. 2010. Characterization and geochemical-geotechnical properties of granite sawdust produced by the dimension stone industry of O Porrino (Pontevedra, Spain). Quarterly Journal of Engineering Geology and Hydrogeology, 43, 141-155.

Bednárik, M. and Kohút, I. 2012. Three-dimensional colour functions for stress state visualisation. Computers & Geosciences, 48, 117-125.

Bernabé, Y. 1991. Pore geometry and pressure dependence of the transport properties in sandstones. Geophysics, 56, 436-446.

Best A.I., Sothcott J. and McCann C. 2007. A laboratory study of seismic velocity and attenuation anisotropy in near-surface sedimentary rocks. Geophysical Prospecting, 55, 609-625.

Blake, O.O. and Faulkner, D.R. 2016. The effect of fracture density and stress state on the static and dynamic bulk moduli of Westerly granite. Journal of Geophysical Research: Solid Earth, 121, 2382–2399.

Cai M. 2010. Practical estimates of tensile strength and Hoek–Brown strength parameter m_i of brittle rocks. Rock Mechanics and Rock Engineering, 43, 167-184.

Canal J., Delgado J., Falcón I., Yang Q., Juncosa R. and Barrientos V. 2013. Injection of CO_2-Saturated Water through a Siliceous Sandstone Plug from the Hontomin Test Site (Spain): Experiment and modeling. Environmental Science & Technology, 47, 159-167.

Chichinina T., Obolentseva I., Gik L., Bobrov B. and Ronquillo-Jarillo G. 2009. Attenuation anisotropy in the linear-slip model: Interpretation of physical modeling data. Geophysics, 74, WB165-WB176.

Churcher P.L., French P.R., Shaw J.C. and Schramm L.L. 1991. Rock properties of Berea sandstone, Baker dolomite and Indiana limestone, SPE International Symposium on Oilfield Chemistry Anaheim, CA, 20-22 February, SPE 21044.

Eissa, E.A. and Kazi, A. 1988. Relation between static and dynamic Young's moduli of rocks. International Journal of Rock Mechanics and Mining Sciences & Geomechanics Abstracts 25, 479-482.

Ellis M.H., Sinha M.C., Minshull T.A., Sothcott J. and Best A.I. 2010. An anisotropic model for the electrical resistivity of two-phase geologic materials. Geophysics, 75, E161–E170.

Falcon-Suarez I., North L. and Best A. 2014. Experimental rig to improve the geophysical and geomechanical understanding of CO_2 reservoirs. Energy Procedia, 59, 75-81.

Farrell N.J.C., Healy D. and Taylor C.W. 2014. Anisotropy of permeability in faulted porous sandstones. Journal of Structural Geology, 63, 50-67.

Fetter C.W. 1993. Contaminant Hydrogeology. 2nd edition. Macmillan Publishing Company, New York.

Fjær, E. 2009. Static and dynamic moduli of a weak sandstone. Geophysics, 74, WA103-WA112.

Fjær, E., Stroisz, A.M. and Holt, R.M. 2013. Elastic Dispersion Derived from a Combination of Static and Dynamic Measurements. Rock Mechanics and Rock Engineering, 46, 611-618.

Fortin, J., Guéguen, Y. and Schubnel, A. 2007. Effects of pore collapse and grain crushing on ultrasonic velocities and Vp/Vs. Journal of Geophysical Research, 112, B08207.

Fortin J., Schubnel A. and Guéguen Y. 2005. Elastic wave velocities and permeability evolution during compaction of Bleurswiller sandstone. International Journal of Rock Mechanics & Mining Sciences, 42, 873–889.

Fredrich J.T., Greaves K.H. and Martin J.W. 1993. Pore geometry and transport properties of Fontainebleau sandstone. International Journal of Rock Mechanics and Mining Sciences & Geomechanics Abstracts, 30, 691-697.

Gaus I. 2010. Role and impact of CO_2-rock interactions during CO_2 storage in sedimentary rocks. International Journal of Greenhouse Gas Control, 4, 73-89.

Hakala M., Kuula H. and Hudson J.A. 2007. Estimating the transversely isotropic elastic intact rock properties for in situ stress measurement data reduction: A case study of the Olkiluoto mica gneiss, Finland. International Journal of Rock Mechanics and Mining Sciences, 44, 14-46.

Hangx S.J.T., Spiers C.J. and Peach C.J. 2010. Creep of simulated reservoir sands and coupled chemical-mechanical effects of CO_2 injection. Journal of Geophysical Research: Solid Earth, 115, B09205.

Hernández J.M., Pujalte V., Robles S. and Martín-Closas C. 1999. División estratigráfica genética del Grupo Campóo (Malm-Cretácico Inferior, SW Cuenca Vascocantábrica). Revista de la Sociedad Geológica de España, 12, 377-396.

Hoek E. and Brown E.T. 1980. Underground Excavations in Rock. The Institute of Mining and Metallurgy, London.

Hoek E., Carranza-Torres C. and Corkum B. 2002. Hoek-Brown criterion–2002 edition, Proc. NARMS-TAC Conference, Toronto, Extended Abstracts, 267-273.

ISRM 1978. Suggested methods for determining the strength of rock materials in triaxial compression. International Journal of Rock Mechanics and Mining Sciences & Geomechanics Abstracts, 15, 99-103.

ISRM 1983. Suggested methods for determining the strength of rock materials in triaxial compression: Revised version. International Journal of Rock Mechanics and Mining Sciences & Geomechanics Abstracts, 20, 285-290.

King, M.S. 1983. Static and dynamic elastic properties of rocks from the Canadian shield. International Journal of Rock Mechanics and Mining Sciences & Geomechanics Abstracts, 20, 237-241.

King M.S. 2009. Recent developments in seismic rock physics. International Journal of Rock Mechanics and Mining Sciences, 46, 1341-1348.

Klein E., Baud P., Reuschlé T. and Wong T.F. 2001. Mechanical behaviour and failure mode of Bentheim sandstone under triaxial compression. Physics and Chemistry of the Earth, Part A: Solid Earth and Geodesy, 26, 21-25.

Krevor S.C., Pini R., Zuo L. and Benson S.M. 2012. Relative permeability and trapping of CO_2 and water in sandstone rocks at reservoir conditions. Water Resources Research, 48, W02532.

Kutchko B.G., Strazisar B.R., Lowry G.V., Dzombak D.A. and Thaulow N. 2008. Rate of CO_2 attack on hydrated class-H well cement under geologic sequestration conditions. Environmental Science & Technology, 42, 6237-6242.

Lau J.S. and Chandler N.A. 2004. Innovative laboratory testing. International Journal of Rock Mechanics and Mining Sciences, 41, 1427-1445.

Le Guen, Y., Renard, F., Hellmann, R., Brosse, E., Collombet, M., Tisserand, D. and Gratier, J.P. 2007. Enhanced deformation of limestone and sandstone in the presence of high fluids. Journal of Geophysical Research: Solid Earth 112, B05421.

Lei X. and Xue Z. 2009. Ultrasonic velocity and attenuation during CO_2 injection into water-saturated porous sandstone: Measurements using difference seismic tomography. Physics of the Earth and Planetary Interiors, 176, 224-234.

Liu F., Lu P., Griffith C., Hedges S.W., Soong Y., Hellevang H. and Zhu C. 2012. CO_2–brine–caprock interaction: Reactivity experiments on Eau Claire shale and a review of relevant literature. International Journal of Greenhouse Gas Control, 7, 153-167.

Louis, L., Robion, P. and David, C. 2004. A single method for the inversion of anisotropic data sets with application to structural studies. Journal of Structural Geology 26, 2065–2072.

Lu P., Fu Q., Seyfried Jr. W.E., Hereford A. and Zhu C. 2011. Navajo sandstone-brine-CO_2 interaction: implications for geological carbon sequestration. Environmental Earth Sciences, 62, 101-118.

Martin C.D. and Chandler N.A. 1994. The progressive fracture of Lac du Bonnet granite. International Journal of Rock Mechanics and Mining Sciences & Geomechanics Abstracts, 31, 643-659.

Martínez J.M. and Schmitt D.R. 2013. Anisotropic elastic moduli of carbonates and evaporites from the Weyburn-Midale reservoir and seal rocks. Geophysical Prospecting, 61, 363-379.

McCann C. and Sothcott J. 1992. Laboratory measurements of the seismic properties of sedimentary rocks. Geological Society, London, Special Publications, 65, 285-297.

Mikhaltsevitch V., Lebedev M. and Gurevich B. 2014. Measurements of the elastic and anelastic properties of sandstone flooded with supercritical CO_2. Geophysical Prospecting, 62, 1266-1277.

Nakagawa S., Kneafsey T.J., Daley T.M., Freifeld B.M. and Rees E.V. 2013. Laboratory seismic monitoring of supercritical CO_2 flooding in sandstone cores using the Split Hopkinson resonant bar technique with concurrent X-ray computed tomography imaging. Geophysical Prospecting, 61, 254-269.

Nakatsuka Y., Xue Z., Garcia H. and Matsuoka T. 2010. Experimental study on CO_2 monitoring and quantification of stored CO_2 in saline formations using resistivity measurements. International Journal of Greenhouse Gas Control, 4, 209-216

Nguyen V.H., Gland N., Dautriat J., David C., Wassermann J. and Guélard J. 2013. Compaction, permeability evolution and stress path effects in unconsolidated sand and weakly consolidated sandstone. International Journal of Rock Mechanics and Mining Sciences, 67, 226 - 239.

Nicksiar M. and Martin C.D. 2012. Evaluation of Methods for Determining Crack Initiation in Compression Tests on Low-Porosity Rocks. Rock Mechanics and Rock Engineering, 45, 607-617.

Njiekak, G., Schmitt, D.R., Yam, H., Kofman, R.S., 2013. CO2 rock physics as part of the Weyburn-Midale geological storage project. International Journal of Greenhouse Gas Control, 16, S118-S133.

North L., Best A.I., Sothcott J. and MacGregor L. 2013. Laboratory determination of the full electrical resistivity tensor of heterogeneous carbonate rocks at elevated pressures. Geophysical Prospecting, 61, 458-470.

North L.J. and Best A.I. 2014. Anomalous electrical resistivity anisotropy in clean reservoir sandstones. Geophysical Prospecting, 62, 1315-1326.

Oh J., Kim K.-Y., Han W.S., Kim T., Kim J.-C. and Park E. 2013. Experimental and numerical study on supercritical CO_2/brine transport in a fractured rock: Implications of mass transfer, capillary pressure and storage capacity. Advances in Water Resources, 62, 442-453.

Ojala I.O., Ngwenya B.T. and Main I.G. 2004. Loading rate dependence of permeability evolution in porouos Aeolian sandstones. Journal of Geophysical Research, 109, B01204.

Pini R., Krevor S.C.M. and Benson S.M. 2012. Capillary pressure and heterogeneity for the CO_2/water system in sandstone rocks at reservoir conditions. Advances in Water Resources, 38, 48-59.

Ptak T., Piepenbrink M. and Martac E. 2004. Tracer tests for the investigation of heterogeneous porous media and stochastic modelling of flow and transport - a review of some recent developments. Journal of Hydrology, 294, 122-163.

Rae P.J., Brown E.N. and Orler E.B. 2007. The mechanical properties of poly(ether-ether-ketone) (PEEK) with emphasis on the large compressive strain response. Polymer, 48, 598-615.

Rouquerol J., Avnir D., Fairbridge C.W., Everett D.H., Haynes J.M., Pernicone N., Ramsay J.D.F., Sing K.S.W. and Unger K.K. 1994. Recommendations for the characterization of porous solids. Pure and Applied Chemistry 66, 1739-1758

Rutqvist J. 2012. The geomechanics of CO_2 storage in deep sedimentary formations. Geotechnical and Geological Engineering, 30, 525-551.

Shackelford C.D., Malusis M.A., Majeski M.J. and Stern R.T. 1999. Electrical conductivity breakthrough curves. Journal of Geotechnical and Geoenvironmental Engineering, 125, 260-270.

Schubnel A., Benson P., Thompson B., Hazzard J. and Young R. 2006. Quantifying damage, saturation and anisotropy in cracked rocks by inverting elastic wave velocities. Pure and Applied Geophysics, 163, 947-973.

Sim C.Y. and Adam L. 2015. Are seismic velocity time-lapse changes due to fluid substitution or matrix dissolution? A CO_2 sequestration study at Pohokura Field, New Zealand. SEG Technical Program Expanded Abstracts, 3123-3128.

Song, I. and Renner, J. 2008. Hydromechanical properties of Fontainebleau sandstone: Experimental determination and micromechanical modelling. Journal of Geophysical Research 113, B09211

Song J. and Zhang D. 2012. Comprehensive review of caprock-sealing mechanisms for geologic carbon sequestration. Environmental Science & Technology, 47, 9-22.

Thomsen L. 1986. Weak elastic anisotropy. Geophysics, 51, 1954-1966.

Vialle S. and Vanorio T. 2011. Laboratory measurements of elastic properties of carbonate rocks during injection of reactive CO_2-saturated water. Geophysical Research Letters, 38, L01302.

Wang Z. 2002. Seismic anisotropy in sedimentary rocks, part 1: A single-plug laboratory method. Geophysics, 67, 1415-1422.

Xu X., Hofmann R., Batzle M. and Tshering T. 2006. Influence of pore pressure on velocity in low-porosity sandstone: Implications for time-lapse feasibility and pore-pressure study. Geophysical Prospecting, 54, 565-573.

Xue Z. and Lei X. 2006. Laboratory study of CO_2 migration in water-saturated anisotropic sandstone, based on P-wave velocity imaging. Exploration Geophysics, 37, 10-18.

Xue Z. and Ohsumi T. 2004. Seismic wave monitoring of CO_2 migration in water-saturated porous sandstone. Exploration Geophysics, 35, 25-32.

Zhan X., Schwartz L.M., Nafi-Toksoz M., Smith W.C. and Dale-Morgan F. (2010). Pore-scale modeling of electrical and fluid transport in Berea sandstone.Geophysics 75, F135F142

Zhu W. and Wong T.F. 1996. Permeability evolution in a dilatating rock: Network modelling of damage and tortuosity. Geophysical Research Letters 23, 3099-3102.

Zhu Y. and Tsvankin I. 2006. Plane-wave propagation in attenuative transversely isotropic media. Geophysics, 71, T17-T30.

Zhu Y., Tsvankin I., Dewangan P. and Wijk K.V. 2007. Physical modeling and analysis of P-wave attenuation anisotropy in transversely isotropic media. Geophysics, 72, D1-D7.

Table 1. Chemical composition of the Corvio Sandstone as resulting from XRF analysis

Constituent	wt.%	Constituent	ppm
Na_2O	0.04	Zr	332
K_2O	0.65	Mn	63
CaO	0.07	Ba	65
MgO	0.09	Sr	31
SiO_2	93.36	Rb	13
TiO_2	0.32	Ni	3
Al_2O_3	4.41	Zn	4
Fe_2O_3	0.10	Cu	2
SO_3	0.01	Pb	3

Table 2. Geomechanical characterization of Corvio sandstone.

Sample	ρ_d (kg m^{-3})	ϕ (%)	σ_3 (MPa)	σ_1 (MPa)	E (GPa)	ν	G (GPa)	K (GPa)
Confined compressive strength				*(CoCS)*				
C91	2026.2	22.1	5	90.6	-	-	-	-
C78	2030.2	21.9	10	107.3	14.71	0.34	5.48	15.44
C87	1998.7	23.2	15	129.9	-	-	-	-
C74	2023.4	22.2	30	153.1	14.62	0.34	5.47	14.99
T115	2122.5	18.4	38	181.4	17.54	0.34	6.57	17.72
C64	2052.7	21.1	50	221.9	13.99	0.34	5.23	14.41
Unconfined compressive strength				*(UCS)*				
C1	2008.8	22.7	0.1	36.0	9.33	0.35	3.47	10.08
C4	2022.7	22.2	0.1	41.1	11.11	0.35	4.11	12.39
C8	2032.0	21.9	0.1	43.7	12.04	0.35	4.47	13.12
C11	2021.4	22.3	0.1	43.3	11.09	0.35	4.10	12.65
C12	2030.9	21.9	0.1	44.4	11.38	0.34	4.25	11.63
C15	2025.3	22.1	0.1	35.4	19.72	0.34	7.34	20.90
C21	2035.3	21.8	0.1	41.4	10.81	0.33	4.08	10.36
C25	2037.5	21.7	0.1	43.7	10.99	0.35	4.08	11.94
C26	1990.9	23.5	0.1	39.4	9.47	0.34	3.53	10.01
C32	2032.3	21.9	0.1	42.9	12.03	0.35	4.46	13.29
Tensile strength (Brazilian)			*(TS)**					
C68-1	2043.5	21.4	3.0	-	-	-	-	-
C68-3	2043.5	21.4	1.8	-	-	-	-	-
C75-1	2020.8	22.3	1.9	-	-	-	-	-
C75-2	2020.8	22.3	2.1	-	-	-	-	-
C75-3	2020.8	22.3	2.7	-	-	-	-	-
C76-1	2016.2	22.5	2.3	-	-	-	-	-
C76-2	2016.2	22.5	1.9	-	-	-	-	-
C76-3	2016.2	22.5	2.4	-	-	-	-	-
C77-1	2035.7	21.7	2.2	-	-	-	-	-
C77-2	2035.7	21.7	2.2	-	-	-	-	-
C77-3	2035.7	21.7	3.1	-	-	-	-	-

* TS = -σ_3; Tensile strength is obtained from indirectly from radial compression (Brazilian test)

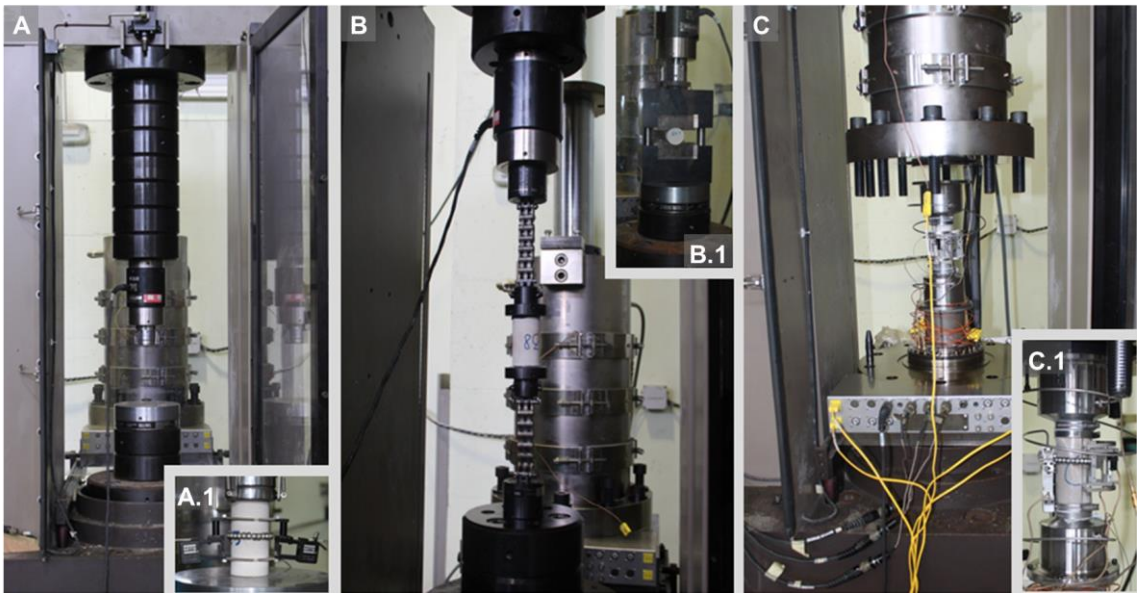

Figure 1. MTS 815 Rock Mechanics Testing System. A, uniaxial configuration and sample (A.1) equipped with extensometers dual-averaging knife-edge type (longitudinal deformation) and chain-type (circumferential deformation); B and B.1, direct and indirect (Brazilian) tensile configurations; C, open-chamber vision of the triaxial configuration and sample (C.1) ready for testing (same type of extensometers as the uniaxial configuration).

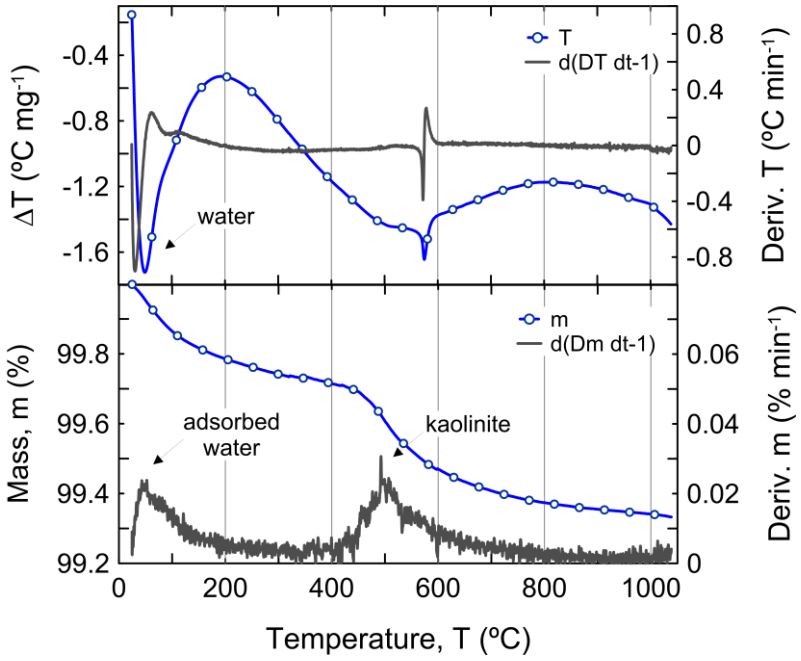

Figure 2. Typical TGA-DTA of Corvio sandstone. The prescribed heating rate was 5 ºK min^{-1} from room temperature 20 ºC to 1050 ºC.

(a)

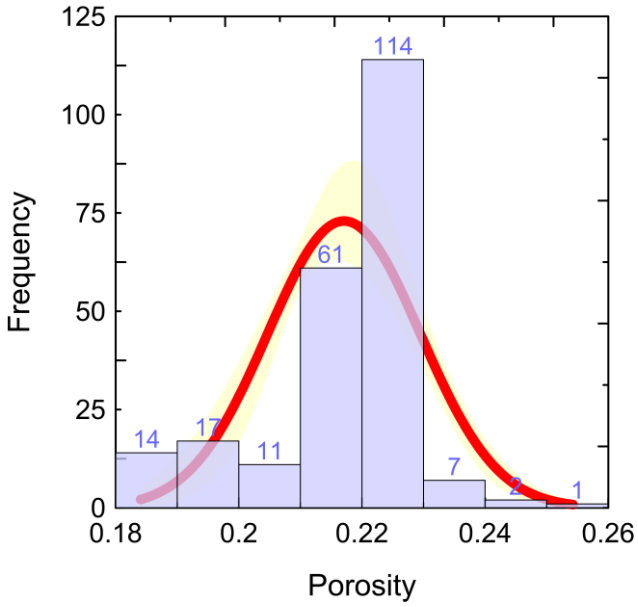

(b)

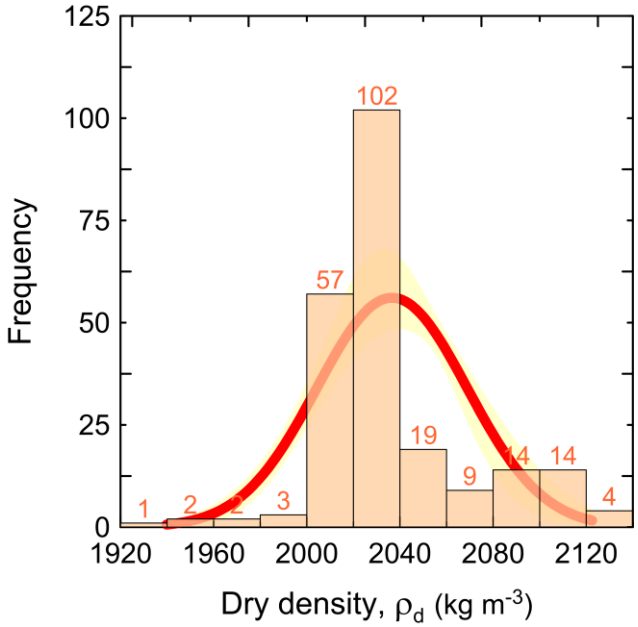

Figure 3. (a) Measured porosity of Corvio sandstone for 227 samples. The line corresponds to a normal distribution function; the shadow represents the associated 95% confidence band; (b) Measured dry density of Corvio sandstone for 227 samples. The line corresponds to a normal distribution function; the shadow represents the associated 95% confidence band.

(a)

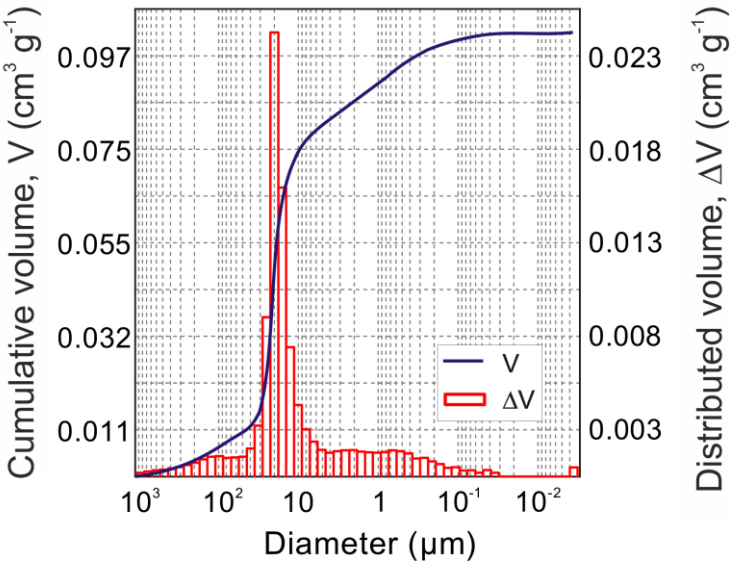

(b)

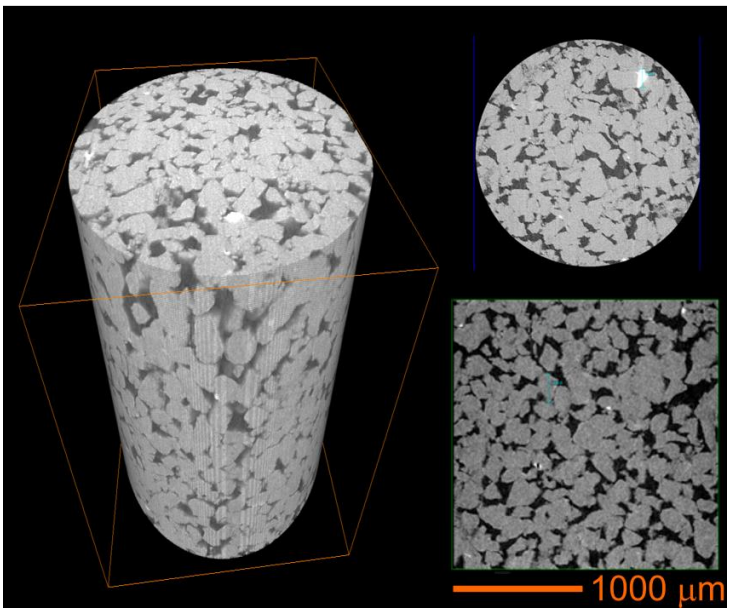

Figure 4. (a) Typical pore size distribution of the Corvio sandstone; (b) X-Ray μCT-scan (full plug, radial and transversal sections; right) of the Corvio sandstone.

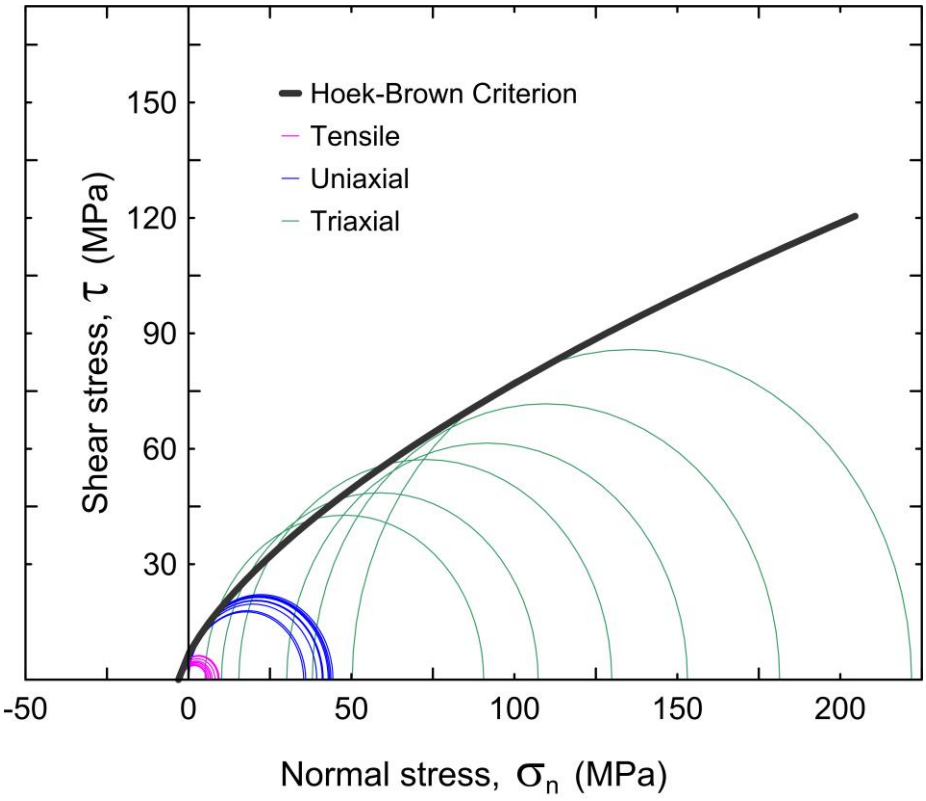

Figure 5. Mohr circles corresponding to the different mechanical tests performed: Tensile (Brazilian tests), Uniaxial (UCS) and Triaxial (CoCS) with the Corvio sandstone. The computed strength envelope, computed from the Hoek-Brown model is also shown.

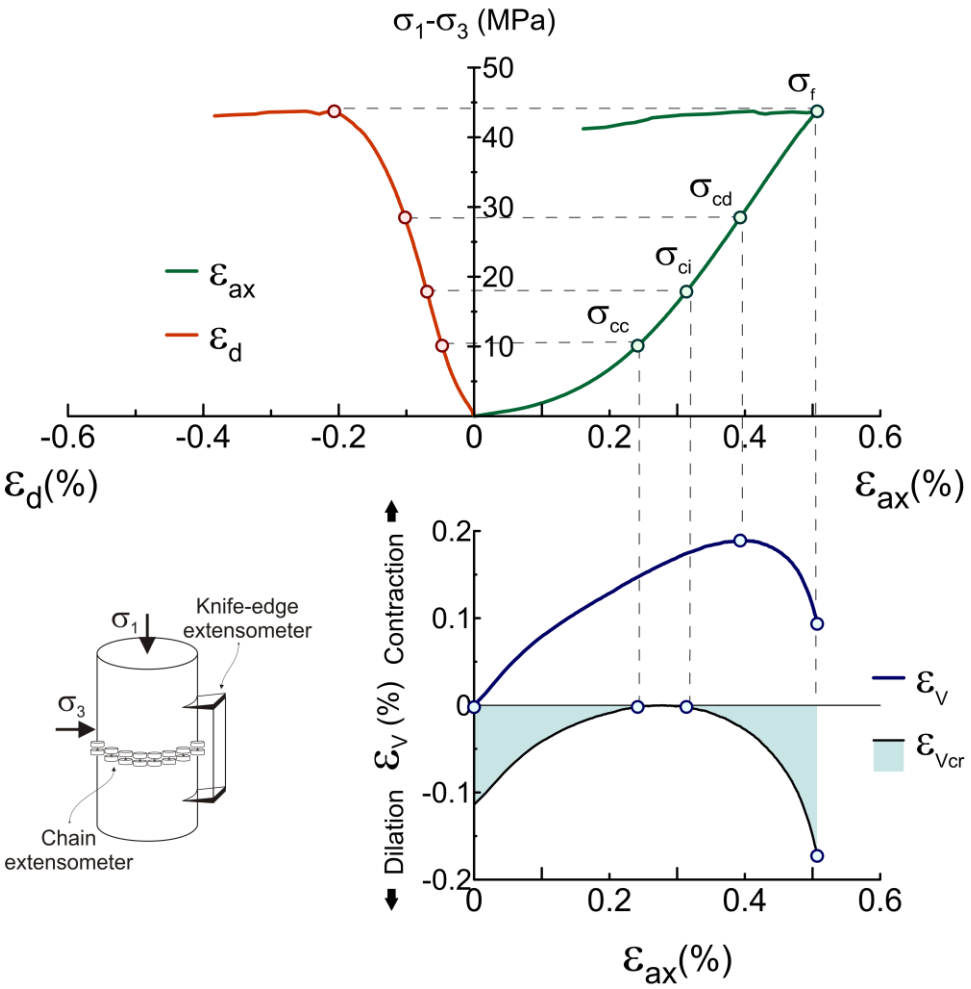

Figure 6. Typical UCS strain-stress curves of the Corvio sandstone and identification of the critical stress states.

(a)

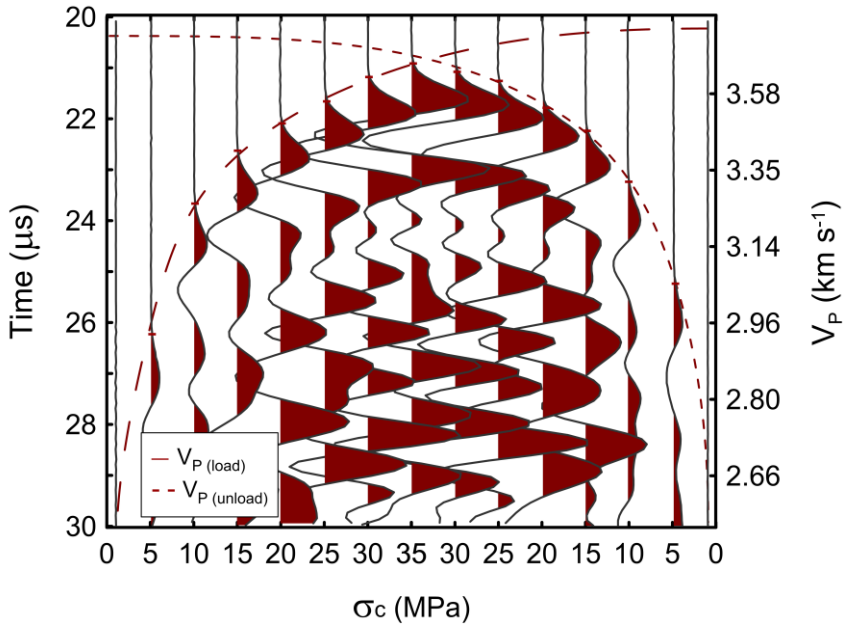

(b)

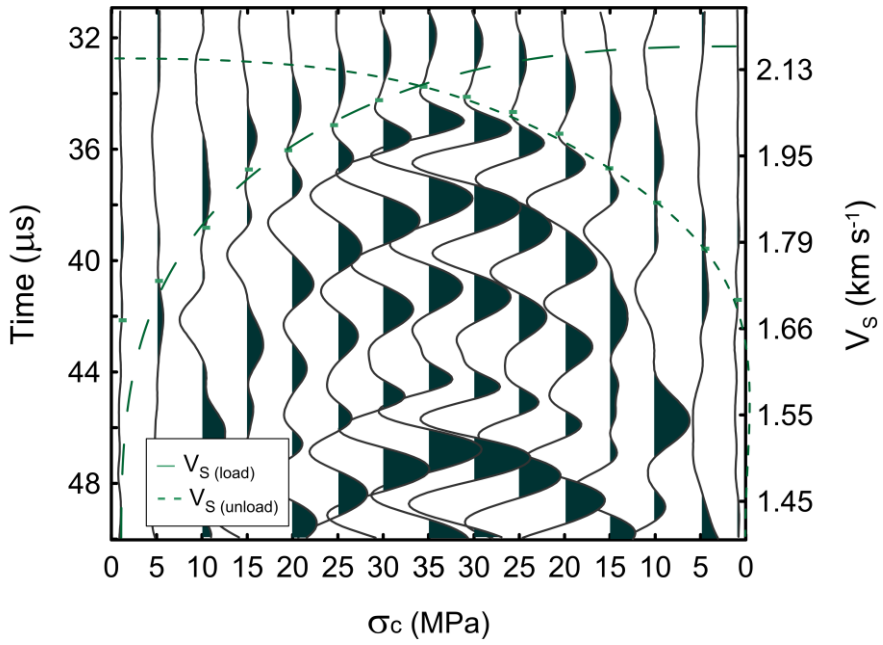

Figure 7. Wiggle-trace plot corresponding to the change in P- (a) and S-wave propagation in Corvio sandstone. Loading/unloading test performed under hydrostatic conditions ($\sigma_1=\sigma_2=\sigma_3$). Discontinuous and dotted lines indicate the first pulse arrival during the loading and unloading sequence, respectively.

(a)

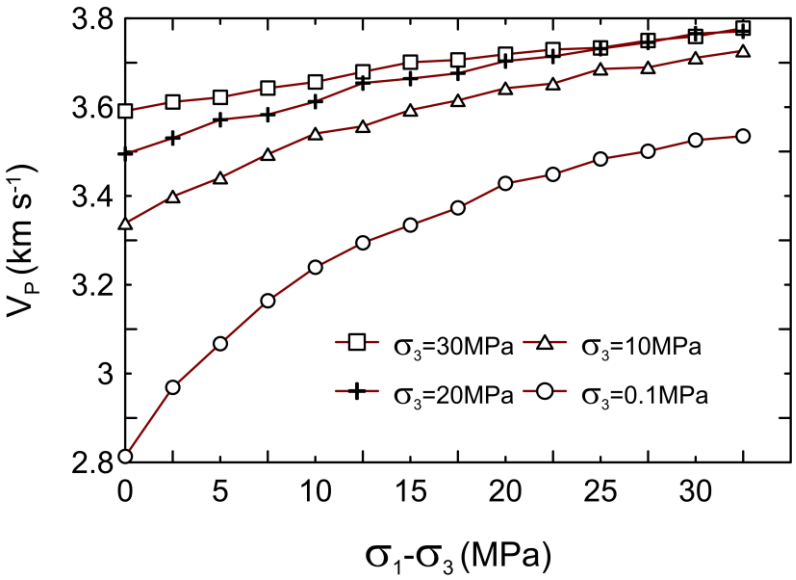

(b)

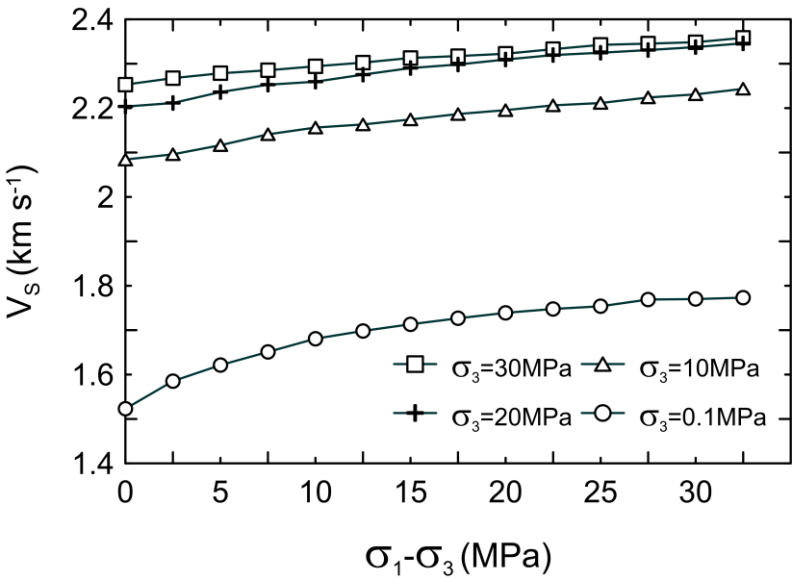

Figure 8. V_p (a) and V_s (b) versus deviatoric stress ($\sigma_1 \neq \sigma_2 = \sigma_3$) for different confining conditions for Corvio sandstone.

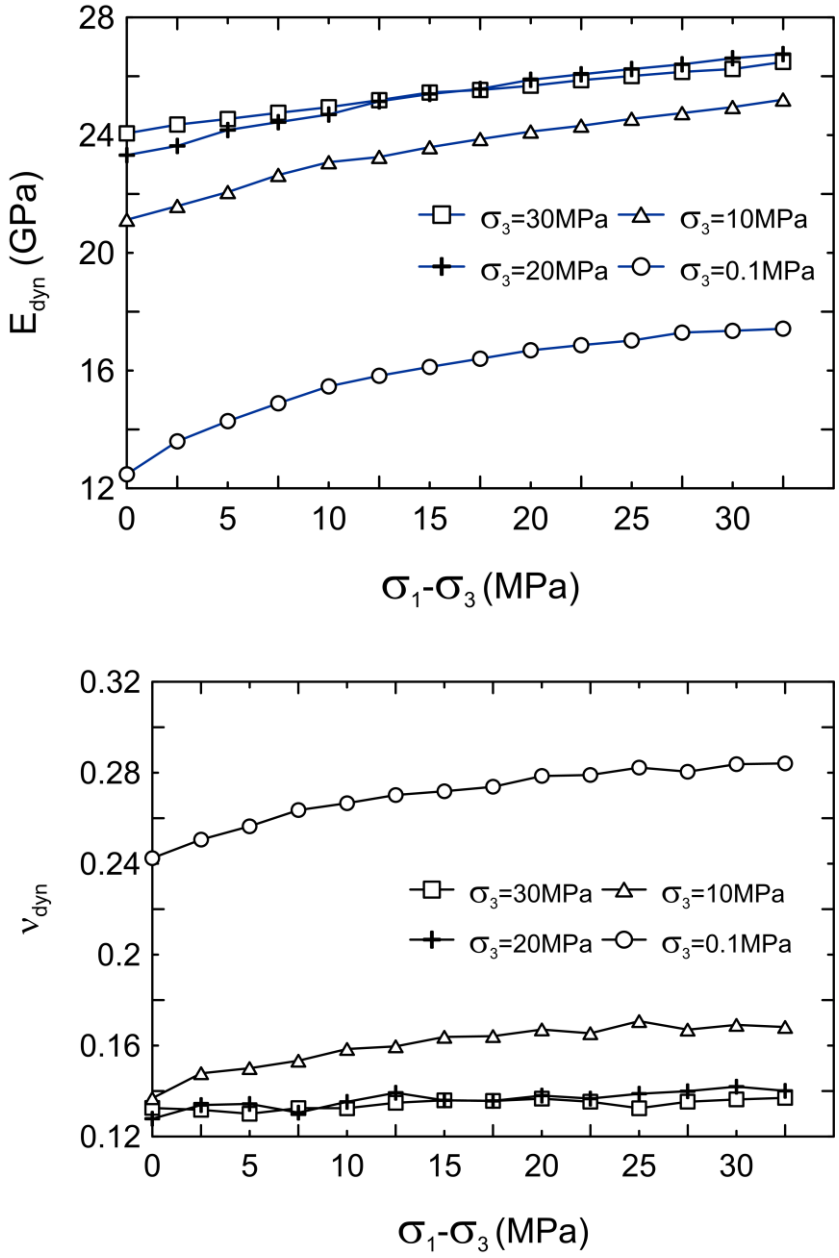

Figure 9. V_p (a) and V_s (b) versus deviatoric stress ($\sigma_1 \neq \sigma_2 = \sigma_3$) for different confining conditions for Corvio sandstone.

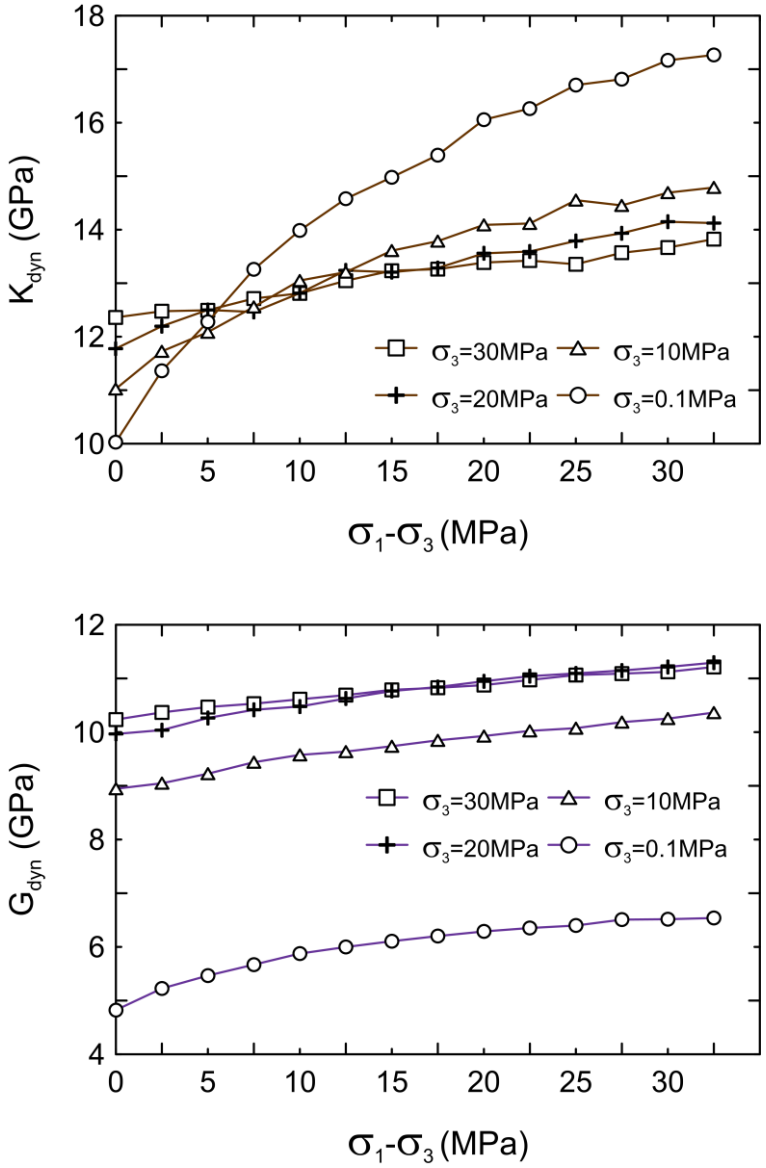

Figure 10. Dynamic Young's modulus, E_{dyn} (a), and dynamic Poisson's ratio, v_{dyn} (b), versus deviatoric stress for different confining conditions ($\sigma_1 \neq \sigma_2 = \sigma_3$), for Corvio sandstone.

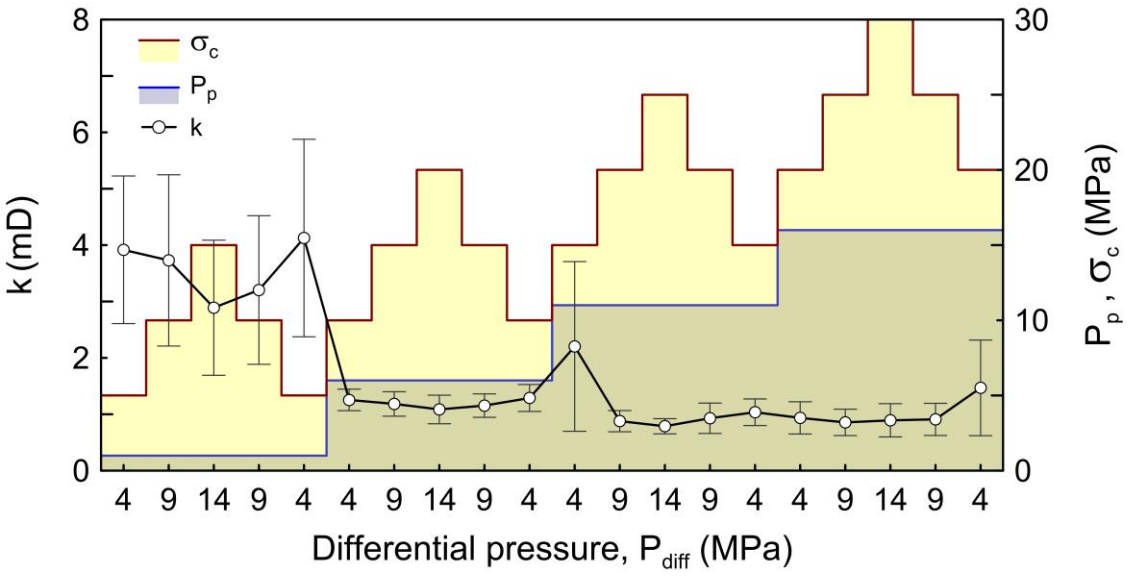

Figure 11. Permeability of Corvio sandstone as resulting from 4 consecutive loading/unloading each one of them performed at constant pore pressure.

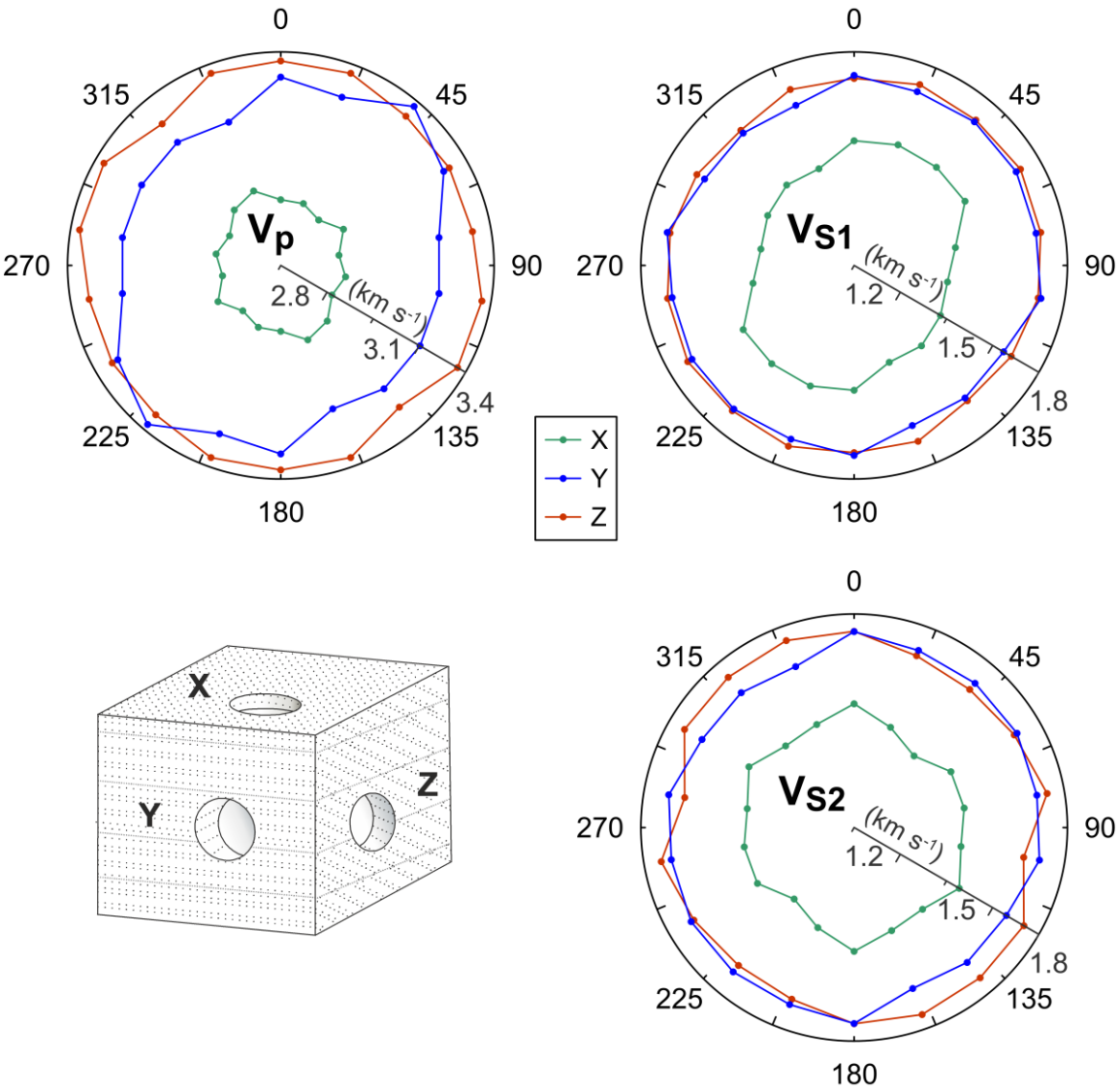

Figure 12. Acoustic wave velocities for the three main orthogonal directions (X-, Y- and Z-plugs) of Corvio sandstone, measured at 20º axially-rotating-steps. The measurements were carried out under unconfined conditions and a load of 1 MPa. The block-diagram illustrates the orientation of each plug.

(a)

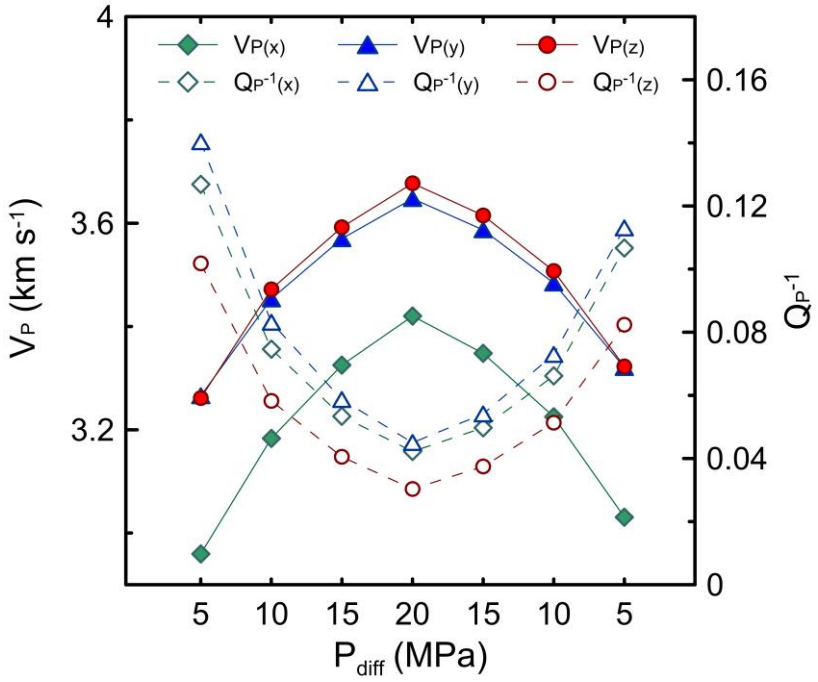

(b)

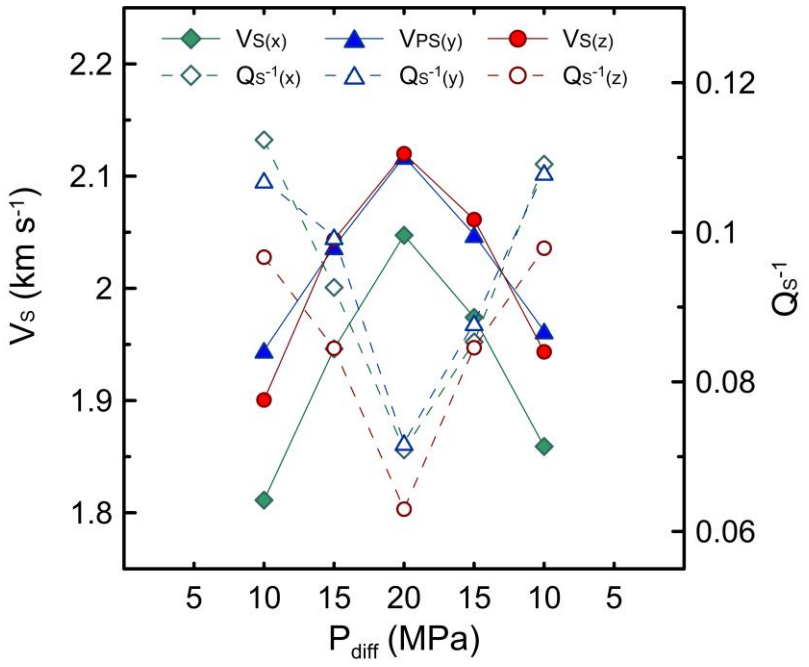

Figure 13. P- (a) and S-wave (b) velocity and their respective attenuation factors for the three main orthogonal directions (X-, Y- and Z-plugs) of Corvio sandstone of Corvio sandstone.

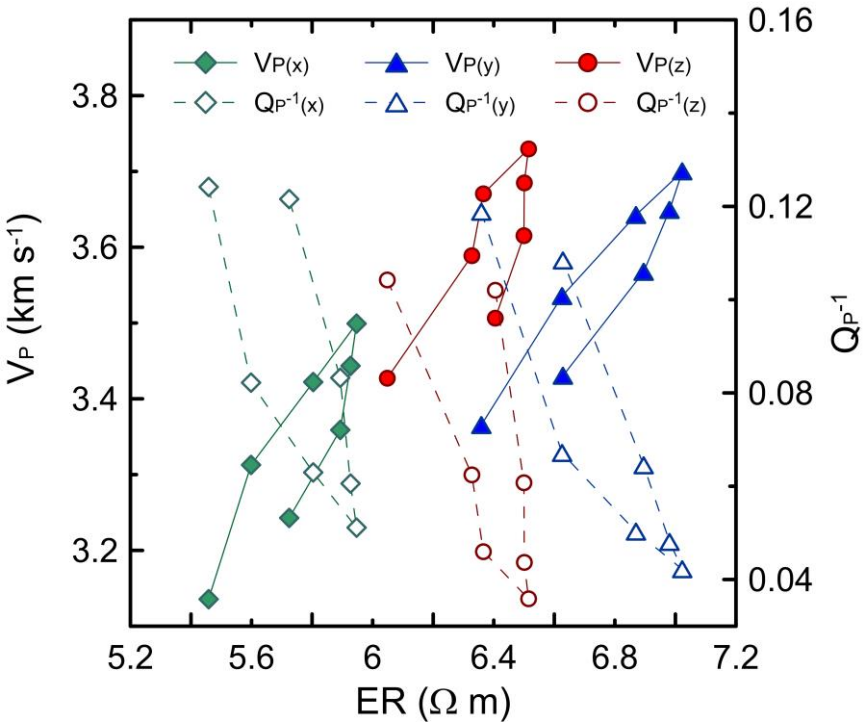

Figure 14. P-wave velocity and attenuation versus bulk electrical resistivity for the three main orthogonal directions (X-, Y- and Z-plugs) of Corvio sandstone.

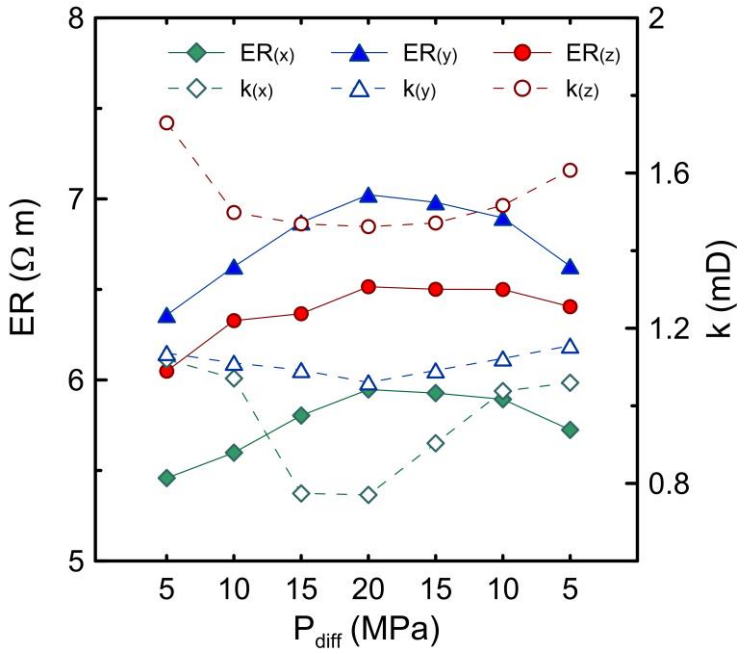

Figure 15. P-wave velocity and attenuation versus bulk electrical resistivity for the three main orthogonal directions (X-, Y- and Z-plugs) of Corvio sandstone.

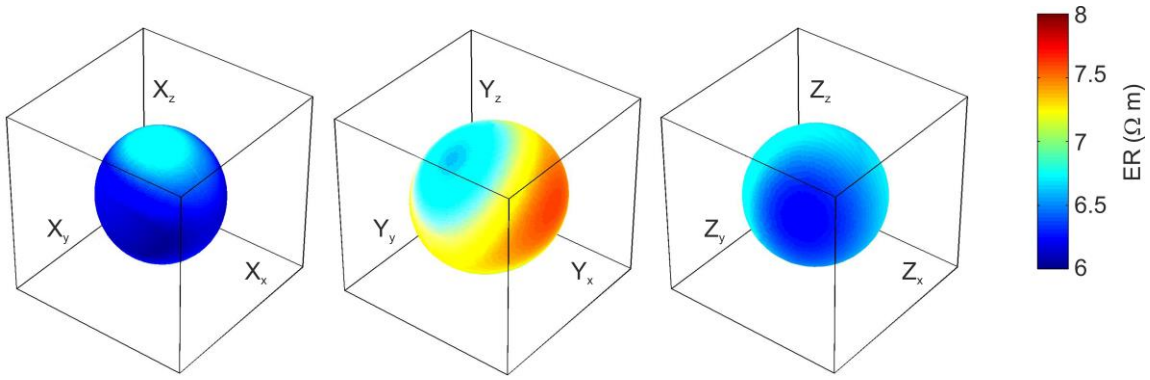

Figure 16. ER anisotropy ellipsoids for the three orthogonal samples of Corvio sandstone (X-, Y- and Zplugs). The radius of each ellipsoid and colour are scaled according to the resistivity values observed along the axial direction of each plug (subscripts x,y and z refer to the three main directions of each sample).

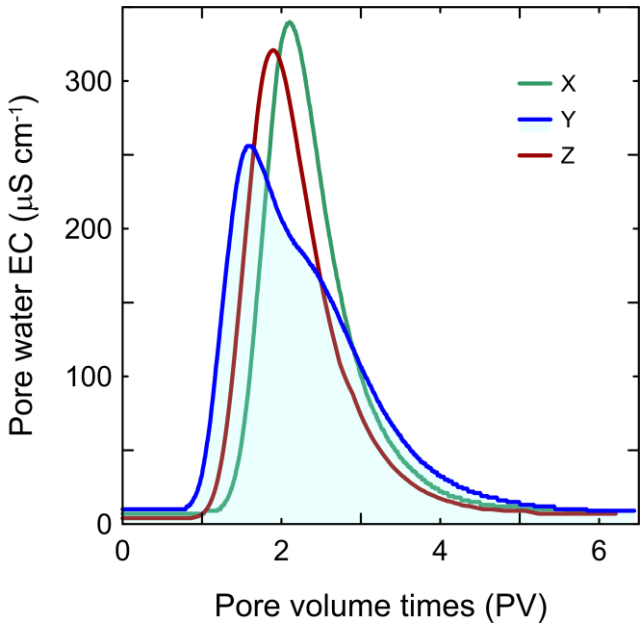

Figure 17. Breakthrough electrical conductivity curves corresponding to pulse-injection tracer tests performed along the three main orthogonal directions (X-, Y- and Z-plugs) of Corvio sandstone.

(a)

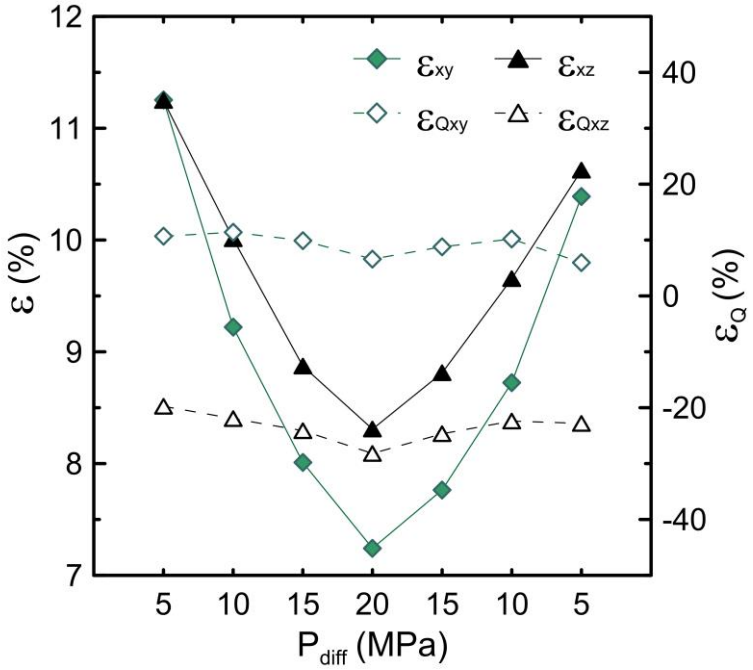

(b)

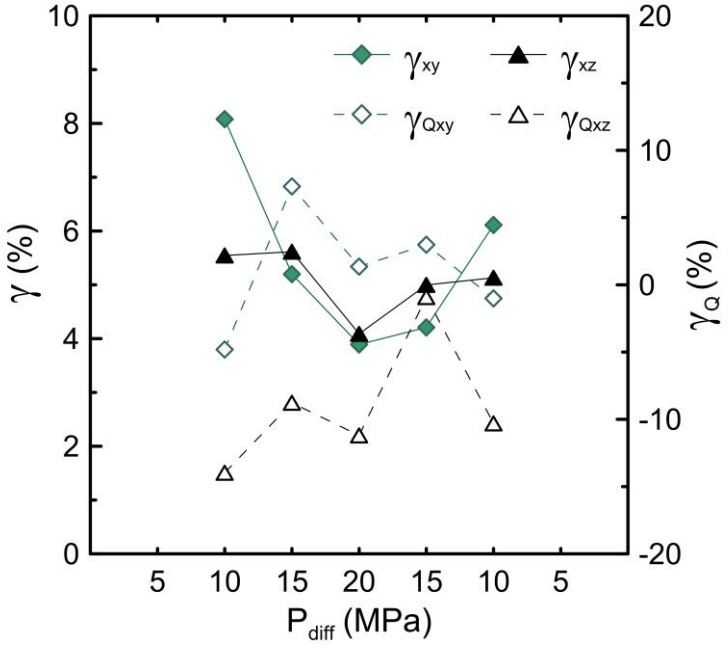

Figure 18. P-wave, ε and ε_Q (a), and S-wave, γ and γ_Q (b), velocity and attenuation anisotropy of the Corvio sandstone.